Molecular Dynamics Simulation Studies of Hydrogen-bond Dynamics in Supercooled Water

Takuma Kikutsuji

MARCH 2022

Molecular Dynamics Simulation Studies of Hydrogen-bond Dynamics in Supercooled Water

A dissertation submitted to

THE GRADUATE SCHOOL OF ENGINEERING SCIENCE

OSAKA UNIVERSITY

in partial fullfillment of the requirements for the degree of

DOCTOR OF PHILOSOPHY IN SCIENCE

by

Takuma Kikutsuji

MARCH 2022

Abstract

Supercooled water exhibits remarkably slow dynamics similar to the behavior observed for various glass-forming liquids. The local order of tetrahedral structures due to hydrogen-bonds (H-bonds) increases with decreasing temperature. Thus, it is essential to clarify the temperature dependence of the H-bond breakage process and its effect on the dynamics deceleration for the whole system.

Chapter 1 provides the general introduction of anomalies in supercooled water.

In Chapter 2, the H-bond breakage process was investigated here using molecular dynamics simulations of TIP4P supercooled water. The two-dimensional (2D) potential of mean force (PMF) is presented using combinations of intermolecular distance and angle between two water molecules. The saddle point of the 2D PMF suggests the presence of the transition state that distinguishes between H-bond and non H-bond states. However, we observed pathways not going through this saddle point particularly at supercooled states, which are due to translational, rather than rotational motions of the molecules. We quantified the characteristic time scales of rotational and translational H-bond breakages. The time scale of translational H-bond breakage shows a non-Arrhenius temperature dependence comparable to that of the H-bond lifetime. In contrast, the time scale of rotational H-bond breakage follows an Arrhenius temperature dependence, where the pathway passes through the saddle point on the 2D PMF profile. This decoupling between rotational and translational processes is relevant for the temperature dependence of the transmission coefficient based on the transition state theory. The translational H-bond breakage is also related to cage-jumps observed in glass-forming liquids, which mostly involve spatially correlated molecules. Our findings warrant further exploration of an appropriate free-energy surface or reaction coordinates beyond the geometrical variables of the water dimer to describe a possible saddle point related to collective jump motions.

Chapter 3 examines the temperature dependence of the H-bond dynamics in supercooled water through the MD simulations using TIP4P/2005 model. First, we investigate the 2D PMF for the H-bond definition using a pair of distance and angle coordinates between two water molecules.

Specifically, we utilize four pairs of the geometrical variables, R-β, r-α, r-γ, and r-ψ, where R and r are the intermolecular O-O and O-H distances, respectively. β and α represent the angles of O-OH and O-HO, respectively, while ψ and γ are angles introduced in terms of the intermolecular O-H vector and the HOH plane of the H-bond acceptor The consistency among the four definitions of H-bond was then examined by identifying the saddle point on the 2D PMF and analyzing the time correlation function of H-bond. It was found over a wide range of temperatures from the ambient to supercooled that the H-bond definition does not affect the H-bond correlation function and correspondingly, the H-bond lifetime τ_{HB}.

Chapter 4 proposes the cage-jump picture with H-bond networks in supercooled water. The slow dynamics of glass-forming liquids is generally ascribed to the cage-jump motion. In the cage-jump picture, a molecule remains in a cage formed by neighboring molecules, and after a sufficiently long time, it jumps to escape from the original position by cage-breaking. The clarification of the cage-jump motion is therefore linked to unraveling the fundamental element of the slow dynamics. Here, we develop a cage-jump model for the dynamics of supercooled water. The caged and jumping states of a water molecule are introduced with respect to the H-bond rearrangement process, and describe the motion in supercooled states. It is then demonstrated from the molecular dynamics simulation of the TIP4P/2005 model that the characteristic length and time scales of cage-jump motions provide a good description of the self-diffusion constant that is determined in turn from the long-time behavior of the mean square displacement. Our cage-jump model thus enables to connect between H-bond dynamics and molecular diffusivity.

Chapter 5 examines a H-bond switching by employing the Markov State Model (MSM). During the H-bond switching, a water hydrogen initially H-bonded with water oxygen becomes H-bonded to a different water oxygen. MSM analysis was applied to trajectories generated from molecular dynamics simulations of the TIP4P/2005 model from a room-temperature state to a supercooled state.

We defined four basis states to characterize the configuration between two water molecules; H-bonded (“H”), unbound (“U”), weakly H-bonded (“w”), and alternative H-bonded (“a”) states.

A 16×16 MSM matrix was constructed, describing the transition probability between states composed of three water molecules. The mean first-passage time of the H-bond switching was estimated by calculating the total flux from the HU to UH states. It is demonstrated that the temperature dependence of the mean first-passage time is in accordance with that of the H-bond lifetime determined from the H-bond correlation function. Furthermore, the flux for the H-bond switching is decomposed into individual pathways that are characterized by different forms of H-bond configurations of trimers. The dominant pathway of the H-bond switching is found to be a direct one without passing through such intermediate states as "w" and "a", the existence of which becomes evident in supercooled water. The pathway through "w" indicates a large reorientation of the donor molecule. In contrast, the pathway through "a" utilizes the tetrahedral H-bond network, which is revealed by the further decomposition based on the H-bond number of the acceptor molecule.

The general conclusion are given in Chapter 6.

Contents

Chapter 1

General Introduction

1.1 Anomalies in supercooled water

Water has many anomalies, such as a maximum density at 4 C$^\circ$ in the liquid state, high surface tension, and high melting point [1]. These anomalies are thought to originate from the hydrogen bonds (H-bonds) that govern molecular structures. The anomalies in the molecular structure and dynamics are enhanced in the supercooled state, where the effect of H-bonds is significant.

The glass state of water is below the deeply supercooled state, where the intermolecular structure is disordered as in the liquid state, but the diffusive motion is stopped as in the solid-state. Glass transition is induced in a thermodynamically metastable state. The time dependency of the transition point is a controversial problem because the transition point shifts depending on the cooling rate. In general, there is no significant change in the intermolecular structure near the glass transition point, but there is a dramatic reduction in the dynamic properties. Therefore, the dynamic properties have been actively studied from the supercooled state to near the glass transition point [2–6].Furthermore, water is a glass-forming liquid because of its liquid-liquid transition, and its structure in the glassy state has attracted much attention.

When water is quenched below 130 K, it forms two types of glass with different density states at a given pressure condition: high-density amorphous (HDA) and low-density amorphous (LDA) [7, 8]. This is thought to be because the local structure can be classified into two states by H-bonds, just as there are various phases in the crystal structure. These two phases do not exist only in the glassy state, however, and there is strong support for the argument that even in the supercooled

state, the liquid phase can be classified as low-density liquid (LDL) or high-density Liquid (HDL) [9]. These properties are thought to be related to the anomalous properties of water, but no clear relationship has been revealed. Therefore, it is essential to focus on the H-bonds that govern the intermolecular structure and dynamics in supercooled water to solve these problems [10–25].

The following sections introduce the dynamic anomalies in the undercooled state and structural anomalies of water in the glassy state.

1.2 Anomalies of dynamics in supercooled water

Glass transition is a phase transition induced in a thermodynamically metastable state by a dramatic decrease in the dynamic properties without any significant change in the intermolecular structures. Therefore, the dynamic properties near the glass transition point and in the supercooled state are essential for understanding the nature of glass transition.

When defining the glass transition temperature using the viscosity coefficient η, the temperature at which η is equal to 10^{12} Pa$\cdot$s was defined as the glass transition temperature T_g. The inverse temperature dependence of η, T_g/T, is widely known as the Angell plot [26]. In the Angell plot, it is known that only two significant types of temperature dependence for η appear even when the material or chemical composition is changed.

One is a "strong" liquid in which the temperature dependence of η obeys the Arrhenius law, $\eta(T) \approx \exp(E/T)$, and is found in molecules with strongly preserved intermolecular networks such as silica glass. The other type is "fragile" liquid, where the temperature dependence of the viscosity shows super-Arrhenius behavior at low temperatures. Fragile liquids are observed in liquids with isotropic intermolecular structures, such as o-terphenyl [26]. The Vogel-Fulcher-Tammann equation can classify those two types of glass-forming liquids more clearly

$$\eta(T) = \exp\left(\frac{CT_0}{T - T_0}\right). \tag{1.1}$$

Here, C the fragility index, where a large C is strong and a small C is fragile [27, 28]. Notably,

water exhibits both strong and fragile properties at different temperatures [2].

In addition, dynamics in the supercooled state exhibit a peculiarity called “dynamic heterogeneity ” [29–33]. In a typical liquid, each molecule moves uncorrelated. As the liquid approaches the glassy state, the activation energy of the uncorrelated motion increases, and the liquid is nearly frozen. Instead of uncorrelated motion collective motion dominates in which each molecule is strongly correlated. Collective motions appear non-uniformly in both space and time dimensions and are observed as dynamic heterogeneity in supercooled state. This dynamic heterogeneity causes different behaviors in the mean square displacement (MSD) and self-intermediate scattering function ($F_s(k,t)$) than those of the liquid.

MSD is the mean square value of the distance $\Delta \boldsymbol{r}(t)$ that the numerator has moved during the time t, and is expressed by the following equation:

$$\mathrm{MSD}(t) = \langle \Delta \boldsymbol{r}^2(t) \rangle. \tag{1.2}$$

$F_s(k,t)$ is the following equation obtained by Fourier transform $\Delta \boldsymbol{r}(t)$:

$$F_s(k,t) = \frac{1}{N} \langle \sum_{i=1}^{N} \exp\left(i\boldsymbol{k} \cdot \Delta \boldsymbol{r}_i(t)\right) \rangle \tag{1.3}$$

where k is generally chosen to be the reciprocal of the distance corresponding to the first neighbor shell between molecules.Figure 1.1 shows the MSD and $F_s(k,t)$ from 300 K to 190 K for the Tip4p/2005 model used in this study.

In the supercooled state (in the case of Figure 1.1, below 240 K), a plateau region appears in the middle time range. This plateau is called the “cage effect”, and it appears when the molecules become stuck in the cage formed by the interactions between the surrounding molecules for a certain period and temporarily lose their motility [26,34]. This cage effect is observed in supercooled states and high-density colloidal solutions, such as in systems where the interaction between molecules dominates motility, with both MD simulations and experiments experiments [30, 35–37]. The cage effect is a phenomenon that appears because of dynamic heterogeneity and increases the diffusion

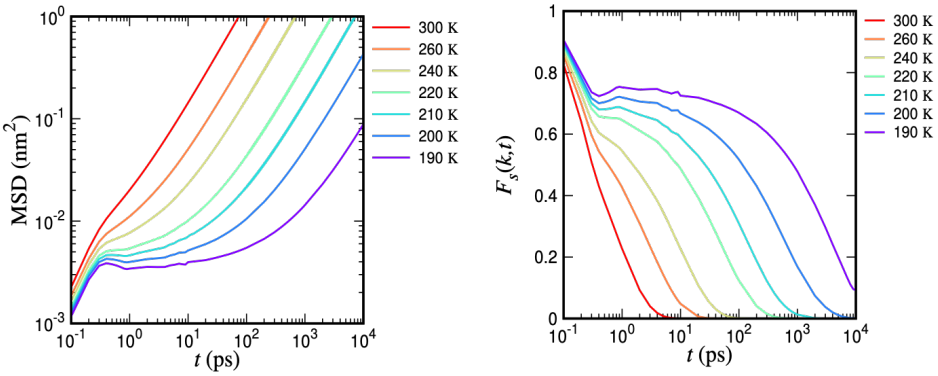

Figure 1.1: MSD and $F_s(k,t)$ for Tip4p/2005 model from 300 K to 190 K. the system consists 8,000 water molecules and density are fixed at 1.0 g/cm^3.

coefficient and relaxation time dramatically. Therefore, understanding the cage effect is key to linking the decrease in mobility (i.e., fragility) with dynamic heterogeneity and understanding the mobility anomaly in supercooled conditions.

1.3 Anomalies of local structures in supercooled water

Various hypotheses have been proposed to explain the anomalous structural and dynamic properties of water in a supercooled state. The existence of a liquid-liquid critical phase transition point is supported by the formation of two pressure dependent amorphous glassy states after quenching from the supercooled state to a lower temperature, and the fact that various physical properties diverge around -45 °C when water is supercooled [38–42].

The supercooled state we observed is the supercritical state of the metastable liquid phase, and it is thought that the two layers are mixed in a critical state. In the supercritical state near the critical point, the critical fluctuation does not disappear immediately, and Widom's line, which is the catch line of the phase transition, shows strong behavior of various physical properties as traces of the phase transition [9, 16, 23]. This hypothesis can explain the divergence of the thermodynamic properties and the singularity of the dynamical properties of water in the supercooled state. However, the liquid-liquid phase transition point is located in the extreme undercooling region "no-

man's land" and has not yet been observed because the liquid solidifies in the general experimental method. Based on the liquid-liquid critical phase transition point, it is assumed that there exists a mixture of two states with different densities in the undercooled state, which we can observe [40]. To overcome the no-man's land problem mentioned above, various measures have been taken in experiments. The most effective method is to reduce crystall size and prevent coagulation. In the early days, the method started by filling a thin capillary tube with water, but it has now reached the point of targeting the water inside the carbon nanotube. In this context, molecular dynamics simulation is a very powerful method to reproduce the supercooled state of water, taking advantage of the fact that water must adopt a tetrahedral structure with very low entropy to crystallize. Nowadays, it is possible to observe time scales down to the μs scale and to calculate temperature scales from room temperature to near the glass transition point.

Recently, it has been suggested that the two states can be defined by H-bonds formed by H-bond. Saito et al. have shown that the number of structures in which the H-bonds are defect-free up to the second neighbor shell increases rapidly after crossing Widom's line at 220 K, and that important structural changes occur at temperatures where the specificity of the dynamics and thermodynamic properties show specificity [16]. Tanaka et al. also clarified that the tetrahedral structure of a system can be classified into two states with different static structure factors in the supercooled state, depending on the ordering of the tetrahedral structure by the H-bond network [2]. Thus, analysis of local structure in supercooled water by molecular simulation has played an important role in the identification of LDL and HDL.

1.4 Local descriptor for water molecules

Under the controversy of the liquid-liquid transition, the local structure in supercooled water has attracted much attention as an index for separating the layers of the liquid phase. Because the tetrahedral structure is dominant in the supercooled state owing to H-bonds, many "local descriptors" have been proposed to characterize the local structure, and the two states in the liquid phase have

been identified according to the discontinuity of the distribution. Local descriptors were used to characterize the local tetrahedral structure.

To evaluate the degree of ordering of the tetrahedral structure using local descriptors, the orientational order parameter q is defined as follows:

$$q = 1 - \frac{3}{8}\sum_{j=1}^{3}\sum_{k=j+1}^{4}(\cos\psi_{jik} + \frac{1}{3})^2, \tag{1.4}$$

where j and k are the indices of the four molecules in proximity to the tagged molecule i, and ψ is the intermolecular angle formed by the oxygen atoms of the water molecule j-i-k [45, 46]. The closer q is to 1, the closer the first neighbor shell is to a tetrahedral structure, and the closer q is to 0, the more disordered the structure is. The use of q allows us to evaluate the local stability in the undercooled state; however, in a sufficiently deep undercooled state, the stable H-bond structure extends to the second neighbor shell [47, 48]. Therefore, in addition to the degree of ordering of the tetrahedral structure, a local descriptor has been developed to evaluate the absence of H-bond defects in the second neighbor shell.

Both d_5 and ξ are descriptors provided to detect molecules entering the first neighbor shell from the second neighbor shell. The d_5 is the distance from the tagged molecule to the fifth nearest molecule, and ξ is the difference between the farthest distance among H-bonded molecules and the closest distance among non-H-bonded molecules [49, 50].

Sasai et al. further clarified the discontinuity in the supercooled state by defining the local structure index (LSI) [51]. LSI $n(i)$ requires the list of nearest neighbor molecule by the oxygen-oxygen distance from the tagged molecule i as follows: $r_1 < r_2 < \cdots < r_{n(i)} < 3.7$ Å $< r_{n(i)+1}$. Here $n(i)$ is the number of molecules that are closer than criterion 3.7 Å. LSI is defined using $n(i)$:

$$\mathrm{LSI} = \frac{1}{n(i)}\sum_{j=1}^{n(j)}\left(\Delta(j) - \bar{\Delta}\right)^2 \tag{1.5}$$

where $\Delta(j) = r_{j+1} - rj$ and $\bar{\Delta}$ is the $\Delta(j)$-average value for $n(i)$.

Many of the local descriptors show a change in the peak position of the distribution function

with decreasing temperature and a double peak near 260-240 K [52]. In addition, the static structure factors classified by ξ exhibit peaks in different parts. In addition, the static structure factors classified by ξ exhibit peaks in different parts, which is evidence of a two-phase mixture in the undercooled state [53].

1.5 H-bond dynamics and structural change of H-bond networks

H-bonds can provide important information not only in supercooled states, but also in various materials such as protein stabilization in water. An H-bond is the bond of a hydrogen atom surrounded by two atoms with high electronegativity (oxygen, nitrogen, fluorine, etc.). The binding energy of an H-bond is 2-10 kcal/mol, which is much weaker than that of a covalent bond, but stronger than the van der Waals force [54]. In the case of a water molecule, an H-bond is formed between the unshared electron pair of an oxygen atom and the hydrogen atom of another water molecule. Although this phenomenon is essentially caused by quantum effects, H-bonds are used as a proxy for molecular configuration in molecular dynamics simulations because they are the dominant factor in the structure and dynamics of large molecular aggregates, such as proteins and biocompatible polymers [55–63].

In molecular dynamics simulations, the most common definition is based on the distance and angle between two molecules [64–67]. The definition of H-bonds is based on the distribution function of molecules in water. In addition, the breaking process in pure water has been studied [68–71]. In room temperature water, H-bonds are switched to compensate for the excess and deficiencies in the H-bond network in the second-neighbor shell. As the H-bonds switch, the donor molecules of the H-bonds undergo large rotational motion [69,70]. This process also occurs in the intermolecular distribution function.

Many properties of water are thought to be caused by H-bonds. In the supercooled state, the tetrahedral structure of H-bonds becomes prominent and anomalous properties and dynam-

ics arise [72–78]. In addition, it has been reported that the breaking time of H-bonds increases dramatically in a supercooled state [79]. This kinetic reduction couples with the inverse of the diffusion coefficient but decouples with the structural relaxation time obtained from the viscosity and self-intermediate scattering functions. This is considered to be the origin of the dynamic heterogeneity in supercooled water represented by the Stokes-Einstein breakdown [80–82]. Against this background, the many-body structure and breaking process due to H-bonding in supercooled water are important issues that are directly related to many mysteries.

1.6 Objective and focus of this dissertation

This study focused on the local structures and dynamics of H-bonds in supercooled water. We elucidate the mechanism of the increase in the H-bond lifetime in the supercooled state and clarify the difference from the breakage process at room temperature. We also explain the effect of the H-bond network on the mobility of the system and link the dramatic reduction in mobility to the structure. We also use three different theories to model the dynamics of H-bonds in the supercooled state. In this way, we try to understand the comprehensive nature of H-bonds by supplementing the parts that each theory can explain.

1.7 Organization of this dissertation

Figure 1.2 shows an outline of the research for each chapter of this study. In the second chapter, we inspected whether the H-bond definition widely used in MD simulations works well in supercooled water using transition state theory and visualized the anomalous H-bond breakage on the two dimensional potential mean force map. Furthermore, the H-bond breakage process allowed us to identify the pathways that determine the H-bond lifetime by revealing differences in the transition time scales. Chapter 3 verifies the temperature dependence of the H-bond lifetime in the all-possible definition based on the geometric conformations of the water dimer. Furthermore, the H-bond breakage process allowed us to identify the pathways that determine the H-bond lifetime

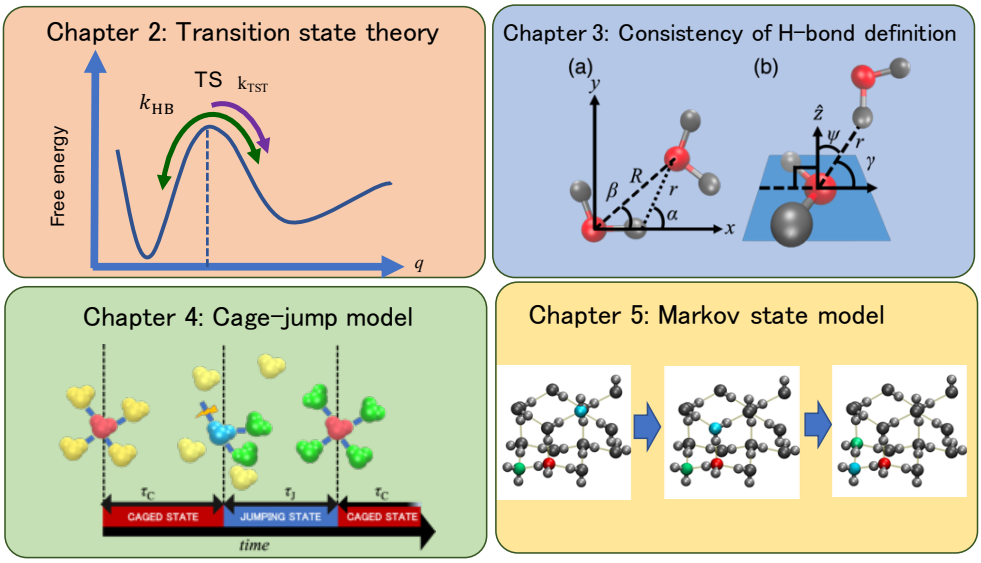

Figure 1.2: Schematic pictures of the research in Chapters 2 through 5.

by revealing differences in the transition time scales. Chapter 4 introduces the cage-jump model based on the continuous-time random walk model, which characterizes dynamic heterogeneity in supercooled water. We divided the short-term dynamics for each molecule according to the H-bond network dynamics and estimated the diffusion coefficient from the short-term dynamics. Chapter 5 analyzes the H-bond switching event from room temperature to a deeply supercooled state using the Markov state model. We identified a new pathway to avoid the loss of H-bond networks in supercooled water by referring to the H-coupling network up to the second adjacent shell.

Chapter 2

How do hydrogen bonds break in supercooled water?: Detecting pathways not going through saddle point of two-dimensional potential of mean force

2.1 Introduction

Liquid water is a complex material that exhibits many anomalous properties [1]. When liquid water is supercooled below its melting temperature, such anomalies become remarkable. The controversial concept of a liquid-liquid transition in deeply supercooled states has attracted much attention from researchers [38–40]. Thus, clarification of the structures and dynamics in supercooled water has been increasingly important in recent years. In particular, water molecules in supercooled water exhibit remarkably slow dynamics similar to that of viscous glass-forming liquids [10–25].

It is generally expected that the hydrogen-bonds (H-bonds) of water molecules play a crucial role in determining their anomalous properties [1]. A large number of experiments and simulations have been carried out to investigate the local structure of H-bonds and the network rearrangement [72–78]. The H-bond is generally defined based on certain structural or energetic criteria of the water-water configuration. Various H-bond definitions in liquid water have been developed for molecular dynamics (MD) simulations [64–67]. A widely used criterion for determining the H-bond is a geometry definition for a pair of water molecules, *i.e.*, a pair of water molecules is considered H-bonded if the intermolecular distance and angle become less than pre-assigned threshold

values. Accordingly, the H-bond correlation function is formulated, allowing quantification of the averaged H-bond lifetime, τ_{HB} [72, 83–86]. Its derivative with respect to time, which is related to the reactive flux, characterizes the H-bond breakage rate [84–86]. As an alternative to τ_{HB} from the correlation function, the distribution function of the H-bond lifetime has been examined using the trajectory based analyses [22, 70, 87–90]. Furthermore, the molecular mechanism of the breakage and reforming of H-bond was comprehensively investigated considering molecular mobility of bifurcated H-bonds [91, 92] and molecular reorientational motions [68–71, 93].

The analysis of H-bond dynamics was also applied in MD simulations of supercooled water [24, 88–90, 93, 94]. The temperature dependence is conventionally analyzed by examining the Arrhenius plot, $\tau_{\mathrm{HB}} \propto \exp(E_{\mathrm{A}}/k_{\mathrm{B}}T)$, where T is the temperature, k_{B} is the Boltzmann constant, and E_{A} is the Arrhenius activation energy of H-bond breakage considering reaction rate theory. The MD studies revealed that τ_{HB} significantly increased with decreasing temperature, showing non-Arrhenius behavior, where E_{A} increased with decreasing the temperature. Collective molecular motions are expected to be a possible scenario by using the analogy with dynamic heterogeneities in glassy systems [95]. However, generally speaking, it is difficult to interpret for E_{A} of supercooled liquids and glasses, *i.e.*, a fragility classification for the temperature dependence of the dynamics [96]. This issue is also relevant with how searching for transition states connecting numerous stable states in the rugged free-energy landscape of complex many-body systems [97, 98]. A study based on this concept was reported using configuration-space-network analysis for H-bond rearrangements [99].

Kumar *et al.* proposed a method to describe the profile for the two-dimensional (2D) potential of mean force (PMF), which is also referred to as the free-energy surface, from the distribution function of the intermolecular distance and angle between two water molecules [64]. This 2D PMF profile enabled the systematic quantification of the distance and angle thresholds, which distinguishes between H-bond and non H-bond regions in classical MD simulations. In Ref. [64], an attempt was made to understand the consistency with H-bond definition based on an electronic structure of water dimer. In addition, profiles of 2D PMF have been also provided by recent ab

initio MD simulations [100, 101]. If the chosen intermolecular distance and angle are treated as the reaction coordinates for the H-bond breakage transition, the dynamics of H-bond breakage is then predicted by the pathway that goes through the saddle point on the 2D PMF profile.

In general, it is challenging to appropriately describe the transition state in various chemical processes in many-body systems, including the H-bond breakage in liquid water investigated here [102–104]. Using a stochastic transition path sampling method for rare events, the kinetic pathway of the H-bond breakage in liquid water was investigated, but little attention was paid to the connection with the 2D PMF [105]. The aim of this study is to address the pathway of H-bond breakage, particularly in supercooled water. In addition, we discuss the mechanism of the non-Arrhenius behavior of the temperature dependence of τ_{HB}.

This study analyses the impact of the the H-bond breakage dynamics in TIP4P supercooled water using MD simulations. The investigated temperatures ranged from 300 K to 190 K at a fixed volume. Using the geometrical variables between water dimer, we calculated the distance-angle distribution function and the associated 2D PMF [64]. From the 2D profile, H-bond and non H-bond regions are distinguished by specifying the saddle point. The H-bond lifetime was quantified from the H-bond correlation function. In addition, the transmission coefficient was calculated based on transition state theory (TST) from reactive flux analysis [106, 107]. and its relationship with the free-energy barrier of the saddle point on the 2D PMF profile was examined.

The present work also focuses on the characteristic time scales of rotational and translational H-bond breakages, which were evaluated from the time dependent H-bond breakage populations. To this aim, the populations in the neighboring regions of the H-bond region were quantified on the 2D PMF profile. The physical implication of the transmission coefficient was examined considering the relationship between rotational and translational H-bond breakages.

2.2 Model and simulations

MD simulations were performed using the TIP4P water model [108]. The various properties of this model have been intensely examined so far. In particular, the comparison with other models including TIP4P/2005 was carefully performed [109]. All the simulations in this work were performed with the GROMACS package [110, 111]. The simulation system contained $N = 1,000$ molecules in the cubic box with the periodic boundary conditions. The mass density was fixed at 1 g/cm^3. Correspondingly, the linear dimension of the system was approximately 3.1 nm. The investigated temperatures were $T = 300$, 260, 240, 220, 210, 200, and 190 K. The system was first equilibrated with the *NVT* ensemble at each temperature for 10 ns. Then, the trajectories for the calculations of various quantities were produced with the *NVE* ensemble for 10 ns ($T \geq 210$ K) and 100 ns ($T \leq 200$ K). A time step of 1 fs was used. For this model, dynamical quantities such as intermediate scattering function and mean square displacement have been reported previously [18] , with which our simulation results were in agreement (data not shown). This indicates that our computational setups are adequate in turn.

The H-bond was investigated by using distance-angle definitions between two water molecules [64]. Specifically, a pair of R and β was chosen, where R represents the O-O intermolecular distance and β is the O-OH intermolecular angle. Note that $0 \leq \beta \leq 180^\circ$. The combined distance-angle distribution function, $g(R,\beta)$, was calculated at each temperature [64]. For this R-β definition, $2\pi\rho R^2 \sin\beta\, g(R,\beta) dR d\beta$ represents the averaged number of O atoms found in the partial spherical shell having dR and $d\beta$ at distance R and angle β from one fixed O atom. Here, ρ is the molecular density of the system. The function $g(R,\beta)$ results in the PMF defined by $W(R,\beta) = -k_{\mathrm{B}}T \ln g(R,\beta)$. This 2D PMF can be regarded as the free-energy surface using reaction coordinates (R,β). The saddle point of $W(R,\beta)$ was numerically determined from the calculations of the gradient $\nabla W(R,\beta)$. Furthermore, the free-energy difference $\Delta G^{\ddagger}$ between the global minimum and saddle point was quantified.

We calculated the time correlation function of the H-bond, $c(t) = \langle h(0)h(t)\rangle / \langle h(0)\rangle$, where $h(t)$

denotes the H-bond operator at a time t [84, 85]. Here, τ_{HB} was determined from $c(t)$ by fitting it to the exponential function $\exp(-t/\tau_{\mathrm{HB}})$.[1] Furthermore, we examined the reactive flux function, $k(t) = -dc(t)/dt$, which quantifies the averaged rate of H-bond breakage [84, 86]. In particular, $k(0)$ is the so-called TST rate constant, k_{TST}, which characterizes the escape rate towards the H-bond broken state at the assumed transition state. We estimated k_{TST} from a finite difference of $c(t)$ with $\Delta t = 1$ fs at each temperature. In contrast, the rate constant for H-bond breakage is approximated by $k = 1/\tau_{\mathrm{HB}}$, which corresponds to the plateau value of $k(t)$ at longer times. These two variables are connected by introducing the transmission coefficient, defined as $\kappa = k/k_{\mathrm{TST}}$, where κ is generally less than unity [106, 107]. The role of the transmission coefficient has been also discussed for H-bond kinetics in liquid water [86].

2.3 Results and discussion

2.3.1 2D PMF and H-bond lifetimes

The 2D PMF contour plots are shown in Fig. 2.1 for $T = 300$ K and 190 K. The H-bond criterion is given by the geometrical condition between the two water molecules [64]. Two molecules are considered H-bonded if the distance-angle relationship is $(0.24\ \mathrm{nm}, 0^\circ) \leq (R, \beta) \leq (0.34\ \mathrm{nm}, 30^\circ)$ (rectangular area indicated in Fig. 2.1). This criterion is mostly consistent with that reported previously [64]. At shorter distance less than $R = 0.24$ nm, the radial distribution functions $g_{\mathrm{OO}}(r)$ vanishes. The position $R = 0.34$ nm corresponds to the first minima of $g_{\mathrm{OO}}(r)$. These threshold values remain unchanged at any temperature, as seen in Fig. 2.1. Figure 2.1 also shows that the temperature dependence of saddle point position is negligible. Instead, the roughness of the landscape becomes larger with decreasing the temperature and the free-energy difference $\Delta G^{\ddagger}$ between the global minimum and saddle point becomes correspondingly larger.

The transition from H-bonded to H-bond breakage states can be generally characterized by the

[1] Note that the stretched exponential function, $\exp[-(t/\tau_{\mathrm{HB}})^{\beta_{\mathrm{HB}}}]$, provided a better fitting for $c(t)$ with the exponent $\beta_{\mathrm{HB}} \approx 0.7$. The obtained τ_{HB} decreased by up to 15% from the value obtained with $\beta_{\mathrm{HB}} = 1$. However, the temperature dependence of τ_{HB} was not influenced overall.

saddle point on the free-energy surface. From our calculations, $(R^{\ddagger}, \beta^{\ddagger}) = (0.32\ \mathrm{nm}, 39^{\circ})$ was obtained (indicated by the gray dot in Fig. 2.1). The H-bond is expected to be broken by increasing β, *i.e.*, by exploiting molecular rotational motions. It is important to note that these 2D plots are not directly linked with k_{TST}, which is the reactive flux at $t = 0$ for a barrier-crossing dynamics with a dividing surface. The introduction of k_{TST} corresponds effectively to adopting a one-dimensional description of the reaction coordinate. On the other hand, a focus in the present work is to determine the TST-type expression, $\exp(-\Delta G^{\ddagger}/k_{\mathrm{B}}T)$, evaluated by referring to the saddle point on the 2D PMF profile. Although this expression does not definitely coincide with k_{TST}, $\Delta G^{\ddagger}$ can be regarded as the Arrhenius activation energy E_{A} when it is independent of temperature over the dividing surface for the reactive flux and κ is unity. Accordingly, the deviation from the Arrhenius behavior of $k = 1/\tau_{\mathrm{HB}}$ has three sources: (1) the temperature dependence of $\Delta G^{\ddagger}$, which is concerned with the entropy of the activation; (2) the dimensionality of the reaction coordinate, which depends on the choice of reaction coordinate; and (3) the temperature dependence of $\kappa(< 1)$, which reflects the detailed dynamics of barrier crossing. These issues are discussed in more detail.

The H-bond correlation function $c(t)$ and reactive flux $k(t)$ are shown in Fig. 2.2. For comparison, the exponential decay curve $\exp(-t/\tau_{\mathrm{HB}})/\tau_{\mathrm{HB}}$ is plotted in Fig. 2.2(b). As mentioned in the end of Sec. 4.2, the decay of $k(t)$ at longer times is characterized by the inverse of H-bond lifetime, $1/\tau_{\mathrm{HB}}$, at each temperature. These behaviors are consistent with previously reported results using SPC/E supercooled water [88, 89]. The temperature dependence of τ_{HB} is plotted in Fig. 2.3, where τ_{HB} increases significantly with decreasing temperature. This drastic increase in τ_{HB}, particularly at supercooled states, has been recently reported using MD simulations [24]. In particular, the temperature dependence shows Arrhenius behaviors, $\exp(E_{\mathrm{A}}/k_{\mathrm{B}}T)$, with different E_{A} values. As shown in Fig. 2.3, E_{A} gradually increases with decreasing the temperature. The E_{A} were 17.9 and 39.6 kJ/mol at the high and low temperature regions, respectively. In contrast, the time scale $\tau_{\mathrm{s}} = 1/k_{\mathrm{TST}}$ associated with the TST rate constant shows the Arrhenius temperature dependence, $\tau_{\mathrm{s}} \propto \exp(E_{\mathrm{s}}/k_{\mathrm{B}}T)$. The estimated Arrhenius activation energy was $E_{\mathrm{s}} = 9.7$ kJ/mol, as shown in Fig. 2.3. Similar values of the activation energy have reported in other liquid water models, where

the average of H-bond persistence lifetime was analyzed [22, 88–90]. This persistence lifetime is relevant with the time scale of TST rate constant [86]. These numerical results are also comparable with experimental values obtained from depolarized Rayleigh scattering [112, 113]. Our observations indicate that the transmission coefficient $\kappa = k/k_{\mathrm{TST}} = \tau_{\mathrm{s}}/\tau_{\mathrm{HB}}$ decreases significantly when the temperature is lowered.

Next, we investigated the relationship between k_{TST} and $\Delta G^{\ddagger}$ (note that k_{TST} is introduced as $k(0)$ in this work). Inset of Fig. 2.3 demonstrates the TST-type relationship, $\tau_{\mathrm{s}} \propto \exp(C\Delta G^{\ddagger}/k_{\mathrm{B}}T))$ with the slope about 0.7; the free-energy barrier corresponding to k_{TST} is underestimated considering the expected value of TST. We again note that the free-energy barrier of 2D PMF is a different quantity from that of the TST framework, which may have resulted in this underestimation. Another possible explanation is H-bond breakages due to non-trivial environmental effects around the tagged H-bonded molecules. Indeed, it has been demonstrated that molecular reorientations are occurred collectively [68]. Such collective motions may have decreased the activation barrier lower than the TST prediction.

From the general expression, $k = \kappa k_{\mathrm{TST}}$, the non-Arrhenius behavior of $\tau_{\mathrm{HB}}(= 1/k)$ and the increase in E_{A} with decreasing temperature are attributed to the temperature dependency of transmission coefficient κ, which considerably decreases with decreasing temperature (see Fig. 2.3). An analogous non-Arrhenius temperature dependence of τ_{HB} has been demonstrated in TIP4P/2005 supercooled water [24]. The physical implication of this is elucidated later.

2.3.2 Temporal development of H-bond distribution function

To reveal the molecular mechanism of H-bond breakage in supercooled water, we examined the change of the geometric structure of two water molecules that are initially H-bonded. To this end, we propose the extension of $g(R,\beta)$ to the time dependent distribution function. Specifically, we introduce the conditional distribution function, $g(R,\beta;t|\mathrm{HB})$, which denotes the distance-angle distribution function of (R,β) at time t for a pair of water molecules located in the H-bonded region at an initial time $t = 0$. Then, the time dependent ratio of the distance-angle distribution function is

defined as follows,

$$G(R,\beta;t) = \frac{g(R,\beta;t|\mathrm{HB})}{g(R,\beta)}. \tag{2.1}$$

This function characterizes the evolution of the spatial correlations of the H-bond over time. Over longer times, the nonequilibrium distribution $g(R,\beta;t=0|\mathrm{HB})$ initially being inside the H-bond region finally recovers to that of the equilibrium distribution $g(R,\beta)$ because of the memory loss. More precisely, we observe $g(R,\beta;t|\mathrm{HB}) \to (N_{\mathrm{HB}}/N)g(R,\beta)$ $(t\to\infty)$, where N is the total number of molecules in the system and N_{HB} denotes the number of averaged accepted H-bonds calculated from integrating $g(R,\beta)$ over the H-bond region (denoted as region HB),

$$N_{\mathrm{HB}} = \int\int_{\mathrm{HB}} 2\pi\rho R^2 \sin\beta g(R,\beta) dR d\beta. \tag{2.2}$$

Note that N_{HB} ranged from from 1.7 ($T = 300$ K) to 2.0 ($T = 190$ K), which is not close to 4 since one of the water molecules has the O atom at the origin and acts only as the H-bond donor, while the H-bond angle β is defined by considering the other water molecule as the H-bond acceptor. We also note that the present investigation is analogous to examining structural relaxation of the selected spectral using the hole-burning technique [114].

Figure 2.4(Multimedia view) shows the time series of $G(R,\beta;t)$. At short time scales, the distribution is firstly elongated towards the angle direction (increasing β). This observation shows that the kinetic pathway of the H-bond breakage mainly passes through the saddle point on the 2D PMF profile. However, as the temperature is decreased, the penetration towards the distance direction (increasing R) becomes more apparent at longer time scales, showing transitions that do not pass through the saddle point. The random, but highly tetrahedral structures lead to frustrations in the H-bond networks in supercooled water. It is possible that these frustrations can be relaxed by collective molecular rearrangements, causing the translational jump motions [33,74,77,115]. Such collective rearrangements require larger activation energies. Furthermore, the 2D PMF using the distance-angle combinations of two-molecule geometry, (R,β), does not show the saddle points consistent with the TST-type behavior.

The translational H-bond breakages are also regarded as the cage effects in glass-forming liquids, suggesting a transient environment around a tagged molecule surrounded by neighboring molecules [35, 116–120]. As demonstrated in various studies, there exists a plateau at an intermediate time regime in the translational mean square displacement of supercooled water, which is a manifestation of cage effects [10, 11, 24, 33, 121]. In fact, the decay of $c(t)$ at the time regime τ_{HB} is dominated by the diffusion process [89]. Furthermore, the coupling between τ_{HB} and the translational diffusion constant D was suggested from the relationship $D \sim {\tau_{\mathrm{HB}}}^{-1}$ in TIP4P/2005 supercooled water [24].

2.3.3 Time scales of rotational and translational H-bond breakages

For the 2D PMF, it is impracticable to calculate the flux across a dividing surface as the kinetic pathway is not along a one-dimensional coordinate. As an alternative, the populations of non H-bond regions adjacent to the H-bonded region were quantified. For this purpose, we define the rectangular H-bond and H-bond breakage regions, as described in Fig. 2.1. The H-bond breakage region due to rotational motions (increasing the angle β) is defined as $(0.24\ \mathrm{nm}, 30^\circ) \leq (R, \beta) \leq (0.34\ \mathrm{nm}, 60^\circ)$, where this region is denoted by R. The H-bond breakage region due to translational motions (increasing the distance R) is also defined as $(0.34\ \mathrm{nm}, 0^\circ) \leq (R, \beta) \leq (0.47\ \mathrm{nm}, 30^\circ)$, denoted as region T. Note that the area of the H-bond breakage region obtained from the integral $2\pi R^2 \sin\beta$ is same for regions R and T. The population of each region was calculated using:

$$N_i(t) = \int\int_i 2\pi\rho R^2 \sin\beta\, g(R, \beta; t|\mathrm{HB}) dR d\beta, \tag{2.3}$$

where i represents the symbol of the region ($i \in \{\mathrm{HB}, \mathrm{R}, \mathrm{T}\}$). Normalization by the number of averaged accepted H-bonds, N_{HB}, is defined as $P_i(t) \equiv N_i(t)/N_{\mathrm{HB}}$. Note that $P_{\mathrm{HB}}(t) = N_{\mathrm{HB}}(t)/H_{\mathrm{HB}}$ is equivalent to the H-bond correlation function $c(t)$ from the definition. We also note that the sum, $P_{\mathrm{HB}}(t) + P_{\mathrm{R}}(t) + P_{\mathrm{T}}(t)$, is not a conserved quantity; it begins as unity at $t = 0$ ($P_{\mathrm{HB}}(0) = 1$ and $P_{\mathrm{R}}(0) = P_{\mathrm{T}}(0) = 0$) and decays to zero as the populations inside the regions R and T at time t will

spontaneously migrate to other non H-bond states afterwards.

Figure 2.5 shows the time evolution of the normalized population, $P_i(t)(= N_i(t)/N_{\mathrm{HB}})$. Both $P_{\mathrm{R}}(t)$ and $P_{\mathrm{T}}(t)$ started from zero and increases with time t. This regime indicates that the inflow due to the H-bond breakage exceeds the outflow towards other non H-bond states. For $P_{\mathrm{R}}(t)$, we observed additional peaks at around $\tau_{\mathrm{lib}} \lesssim 0.1$ ps, which are independent of the temperature, attributed to libration motion. They eventually decay to zero after a peak time, where the outflow exceeds the inflow for longer time scales. That is, the maximum peaks are determined by the balance. Thus, the peak times of $P_{\mathrm{R}}(t)$ and $P_{\mathrm{T}}(t)$ (denoted as τ_{R} and τ_{T}, respectively) can be regarded as the characteristic time scales of irreversible H-bond breakages due to rotational and translational motions, respectively. It should be noted that the pathways going from region R(T) to T(R) were not detected. In fact, the H-bond breakages for time regimes at either τ_{R} or τ_{T} are irreversible for a particular pair of water molecules and two water molecules hardly reform the same H-bond pair. We observed that there existed a population of the translational H-bond breakage, even at higher temperatures. The peak value of $P_{\mathrm{T}}(t)$ becomes comparable to that of $P_{\mathrm{R}}(t)$ with decreasing the temperature. This indicates the increasing number of pathways not going through the saddle point on the 2D PMF profile, particularly for supercooled water.

The temperature dependence of τ_{R} and τ_{T} is plotted in Fig. 2.6. It can be seen that τ_{T} is comparable with τ_{HB} at all studied temperatures. In contrast, the time scale of τ_{R} is about one order of magnitude smaller than τ_{T} although the temperature dependence of τ_{R} shows similar Arrhenius behaviors. These observations indicate that the H-bond lifetime τ_{HB} is dominated by the H-bond breakages caused by translational motions. Finally, this observation $\tau_{\mathrm{T}} \simeq \tau_{\mathrm{HB}}$ results in the following implication for the temperature dependence of κ;

$$\frac{1}{\kappa} = \frac{\tau_{\mathrm{HB}}}{\tau_{\mathrm{s}}} \simeq \tau_{\mathrm{T}} \exp\left(\frac{C\Delta G^{\ddagger}}{k_{\mathrm{B}}T}\right). \tag{2.4}$$

This relationship is direct evidence that the temperature dependence of κ is caused by that of the time scale of H-bond breakage due to translational motions.

2.4 Conclusions

We analyzed the H-bond breakage dynamics in the TIP4P supercooled water considering a geometric definition of the H-bond. We first investigated the temperature dependence of the 2D PMF obtained from the distance-angle distribution function. It was found that the position of the saddle point distinguishing H-bond and non H-bond regions remains unchanged at all studies temperatures, while the free-energy barrier of the saddle point, $\Delta G^{\ddagger}$, gradually increased with decreasing temperature. We showed that the Arrhenius activation energy of τ_{HB} increases with decreasing temperature. In contrast, the TST rate constant k_{TST} of the H-bond breakage approximately followed the Arrhenius temperature dependence. In addition, the TST-type expression, $\exp(C\Delta G^{\ddagger}/k_{\mathrm{B}}T)$, was obtained, where the correction factor C was temperature independent. This suggests a significant decrease in the transmission coefficient κ with decreasing temperature.

To elucidate the molecular mechanism of H-bond breakage, the kinetic pathways of H-bond breakage were studied. In particular, the time dependence of the conditional distance-angle distribution function revealed the pathways that did not go through the saddle point when the system was deeply supercooled, which was attributed to H-bond breakages due to translational motions. This translational H-bond breakage is thought to be associated with the cage-jump motion, which is commonly observed in various glass-forming liquids. In addition, it is proposed that the avalanches of cage-jump motions trigger collective molecular motions, referred to as dynamic heterogeneities. Our observations indicated that such collective motions involving many molecules were not described well by the present 2D PMF using geometric variables defined by the water dimer.

Furthermore, we quantified the time dependent populations of the rotational and translational H-bond breakages. With decreasing temperature, the population of the translational H-bond breakage became comparable to that of the rotational H-bond breakage passing through the saddle point. In particular, the time scale of the translational H-bond breakage τ_{T} became much longer than that of the rotational H-bond breakage τ_{R}. The temperature dependence of the H-bond lifetime τ_{HB} was comparable to that of τ_{T}. This suggests that the H-bond lifetime τ_{HB} is dominated by the

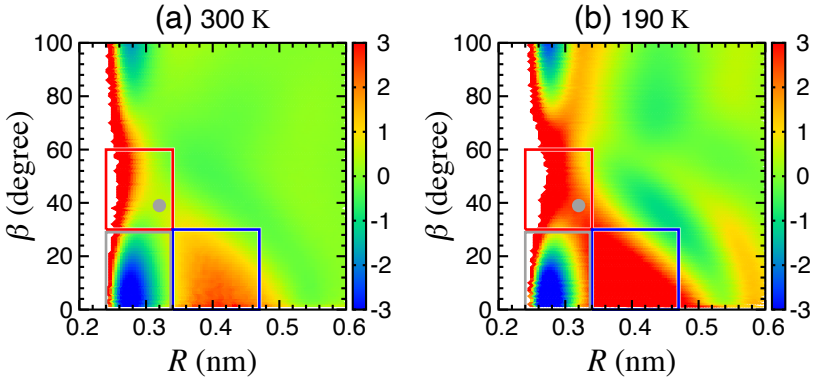

Figure 2.1: Contour plots of the potential of mean force, $W(R,\beta)$, at a temperature of 300 K (a) and 190 K (b). The value of the color bar is normalized by $k_{\mathrm{B}}T$. The saddle point is shown by the gray point. The rectangle indicated by the gray line represents the H-bond region. The areas surrounded by red and blue lines represent the H-bond breakage regions due to rotational and translational motions, respectively (denoted as regions R and T). The region with unsampled configurations is shown in white.

translational motions. In addition, the transmission coefficient κ from unity were explained by the temperature dependence of τ_{T}.

Finally, we note that it is important to investigate whether the 2D PMF associated with H-bonds and their breakages is suitable for supercooled water. In fact, Sciortino *et al.* demonstrated that the bifurcated H-bond configuration promotes H-bond breakages with high mobility [91, 92], which is apparently "hidden" in the 2D PMF drawn for a pair of water molecules; a bifurcated bond can be explicitly described only beyond the pair level. Our observations suggested that there exists another possible saddle point on the 2D PMF profile that reflects the translational H-bond breakage relevant with the bifurcated bonds. Hence, the profile of the PMF might be appropriately transformed, even with the same reaction coordinates, by using information regarding the kinetic pathways from the H-bond to the non H-bond regions. We are currently undertaking further investigations to clarify this issue.

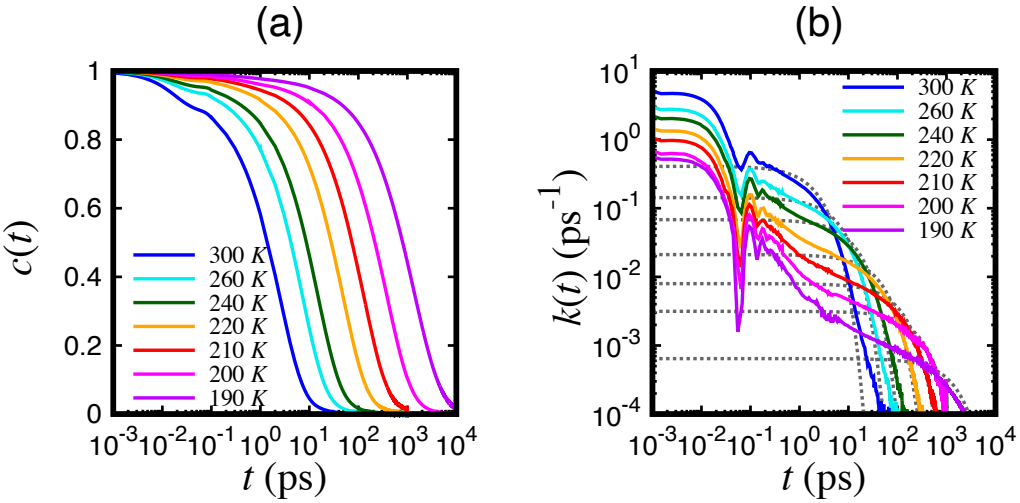

Figure 2.2: (a) H-bond correlation function $c(t)$. (b) Reactive flux $k(t) = -dc(t)/dt$. Dotted curves represent the exponential function $\exp(-t/\tau_{\mathrm{HB}})/\tau_{\mathrm{HB}}$ with H-bond lifetime τ_{HB}.

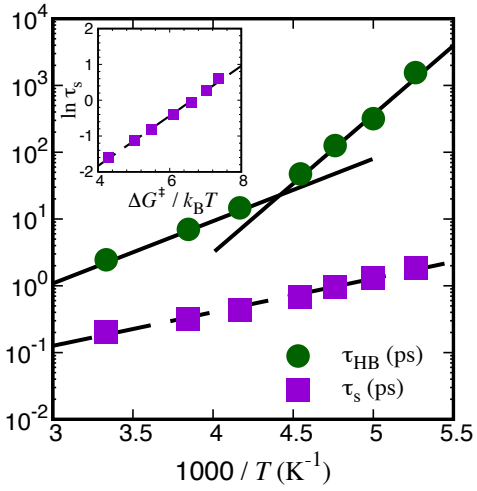

Figure 2.3: H-bond lifetime τ_{HB} and inverse TST rate constant $\tau_s = {k_{\mathrm{TST}}}^{-1}$ vs. inverse temperature $1000/T$. The Arrhenius behavior $\tau_{\mathrm{HB}} \propto \exp(E_{\mathrm{A}}/k_{\mathrm{B}}T)$ in the high and low temperature ranges are shown as two straight lines, with activation energies with $E_{\mathrm{A}} = 17.9$ and 39.6 kJ/mol, respectively. The dashed line shows Arrhenius behavior for $\tau_{\mathrm{s}} \propto \exp(E_{\mathrm{s}}/k_{\mathrm{B}}T)$ with $E_{\mathrm{s}} = 9.7$ kJ/mol. Inset: $\ln \tau_{\mathrm{s}}$ vs. the free-energy barrier of the saddle point $\Delta G^{\ddagger}/k_{\mathrm{B}}T$ on the 2D PMF profile. The dashed straight line is the fitting of $\tau_{\mathrm{s}} \propto \exp(C\Delta G^{\ddagger}/k_{\mathrm{B}}T)$ with a constant $C = 0.7$.

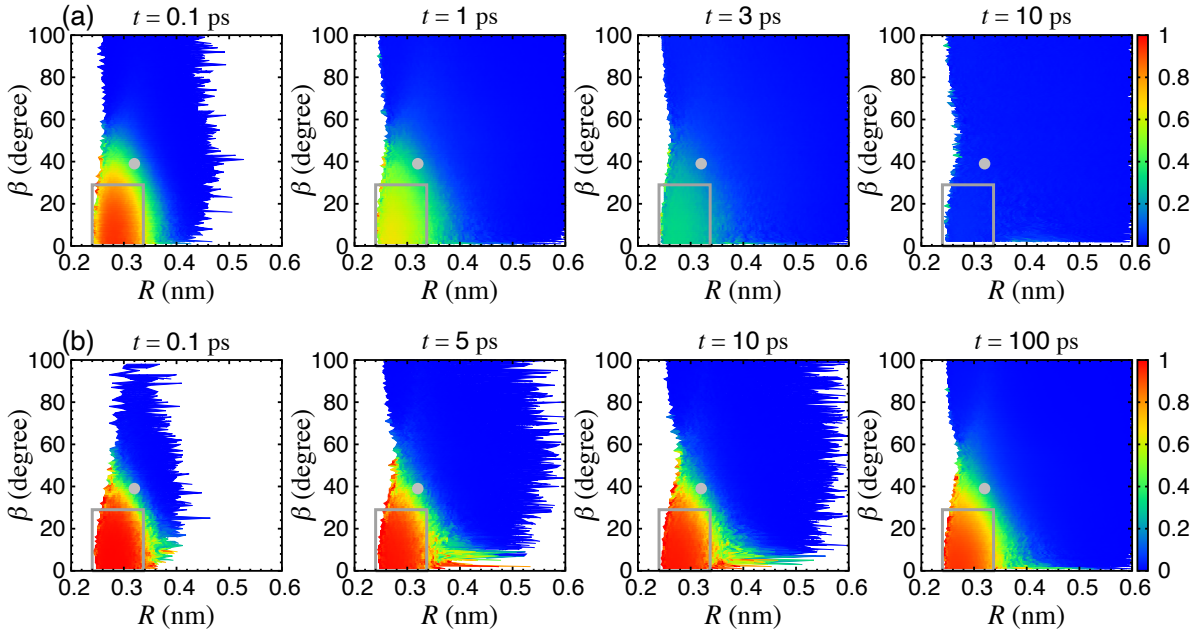

Figure 2.4: Conditional distance-angle distribution function $G(R,\beta;t)$ at temperatures of 300 K (a) and 190 K (b). The saddle point is shown by the gray point. The rectangle indicated by the gray line represents the H-bond region. The region with unsampled configurations is shown in white. (Multimedia view)

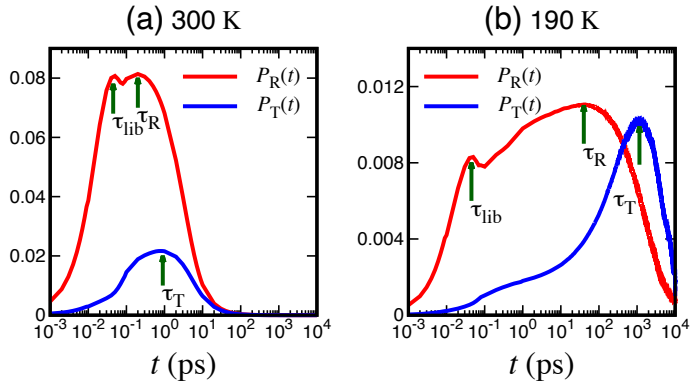

Figure 2.5: Time evolution of the normalized populations $P_{\mathrm{R}}(t)$ and $P_{\mathrm{T}}(t)$ for H-bond breakage regions at temperatures of 300 K (a) and 190 K (b). The H-bond breakage regions (regions R and T) are depicted in Fig. 2.1. Here, τ_{lib}, τ_{R}, and τ_{T} are indicated by arrows.

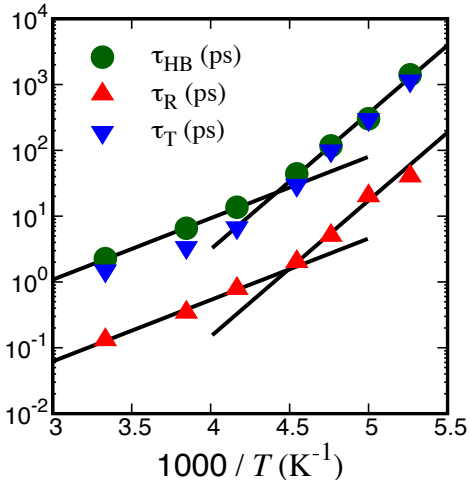

Figure 2.6: Temperature dependence of the maximum times in $P_{\mathrm{R}}(t)$ and $P_{\mathrm{T}}(t)$, as denoted by τ_{R} and τ_{T}, respectively. Comparisons with τ_{HB} are also shown. The straight lines represent Arrhenius behavior $\exp(E_{\mathrm{A}}/k_{\mathrm{B}}T)$ in the high and low temperature ranges with activation energies with $E_{\mathrm{A}} =$ 17.9 and 39.6 kJ/mol, respectively.

Chapter 3

Consistency of geometrical definitions of hydrogen bonds based on the two-dimensional potential of mean force with respect to the time correlation in liquid water over a wide range of temperatures

3.1 Introduction

The elucidation of forming and breaking processes of the hydrogen-bond (H-bond) between water molecules is important to understand the dynamics of liquid water [68, 74, 84–86]. In order to characterize dynamical processes of H-bond, enormous experiments and simulations have been carried out so far [73–78].

When analyzing the H-bond dynamics in classical molecular dynamics (MD) simulations, a geometrical condition is conventionally utilized to define an H-bond between two water molecules. The most frequently used definition focuses on O-O distance and O-OH angle of water dimer [84–86]. It might argued, though, that physical pictures depend on how the H-bond is defined, and thus the consistency among a variety of H-bond definitions has been addressed in terms of the two-dimensional (2D) potential of mean force (PMF) obtained from the distance-angle distribution function [64]. Note that the specific temperature at 300 K is typically investigated. The consistency still needs to be clarified when water is supercooled and the dynamic features for H-bond breakage changes [66]. MD is then a method of choice to examine the consistency since it has been proven

useful to examine the slow dynamics of supercooled water at atomic resolution [10–20, 22–25, 90, 122–125].

In the present work, we conduct MD simulations over a wide range of temperatures from the ambient to supercooled and analyze the H-bond dynamics on the basis of the 2D PMF. We utilize four combinations of distance and angle to define an H-bond, while Ref. [124] reported the results with one of the definitions using the O-O distance and O-OH angle. For each H-bond definition, we first calculate the 2D PMF profile from the distance-angle distribution function. The 2D PMF divides the configurations of a pair of water molecules into the H-bond and non H-bond regions. In particular, we investigate the temperature dependence of the dividing line of the two regions from 300 K to 190 K at a constant density 1 $\mathrm{g/cm^3}$ of TIP4P/2005 model. Next we calculate the H-bond time correlation function, from which the H-bond lifetime τ_{HB} is determined. We discuss the consistency among the four definitions of H-bond on the basis of the temperature dependence of τ_{HB}.

3.2 Model and simulations

MD simulations were performed using the TIP4P/2005 water model [109]. All the simulations in this work were carried out with the GROMACS2016.4 package [110, 111]. The simulation system contained $N = 1,000$ molecules in the cubic box with the periodic boundary conditions. The mass density was chosen at 1 $\mathrm{g/cm^3}$. The cell size of the system was approximately 3.1 nm. The examined temperatures were $T = 300$, 260, 240, 220, 210, 200, and 190 K. The system was first equilibrated with the *NVT* ensemble at each temperature for 100 ns. Then, the trajectories were generated with the *NVE* ensemble for 100 ns for each temperature, from which the 2D PMF and H-bond correlation function were calculated. A time step of 1 fs was used.

The H-bond definition was introduced by using geometrical variables between two water molecules [64]. The geometrical structure representing each variable is shown in Fig. 3.1. In this study, we adopted four combinations of distance and angle for the H-bond definition, R-β, r-α, r-γ, and r-ψ.

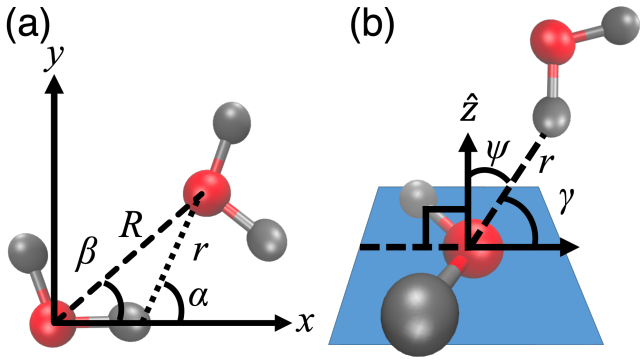

Figure 3.1: Pictorial representation of the distances (R and r) and angles ($\beta, \alpha, \gamma, \psi$) discussed in the text. The $\hat{z}$ axis is perpendicular to the molecular plane.

R and r are the intermolecular distances O-O and O-H, respectively, and β, α, γ, and ψ denote intermolecular angles. β is the O-OH angle, while α represents the angle between the intramolecular O-H vector and the intermolecular O-H vector. γ is the angle between the intermolecular O-H vector from the acceptor O site and the bisector of the acceptor HOH, and ψ refers to the angle of the intermolecular O-H with the line that passes the acceptor O and is perpendicular to the HOH plane.

R-β and r-α definitions place the O site of the H-bond donor at the origin of the coordinate. We thus refer to R-β and r-α definitions as donor definitions. In contrast, the O atom of the H-bond acceptor is located at the origin for r-γ and r-ψ definitions, which are regarded as acceptor definitions. The acceptor definition was introduced to analyze its link with the electronic structure-based H-bond definition [64]. Note that $0^\circ < \beta, \alpha, \gamma < 180^\circ$. Furthermore, ψ usually takes a value of $0^\circ < \psi < 90^\circ$, but the range $-90^\circ < \psi < 0^\circ$ is also examined in this study. The purpose is to precisely characterize the configuration of the H atom of the donor molecule relative to the O atom of the acceptor molecule.

For the donor definitions, $2\pi\rho R^2 \sin\beta g(R,\beta) dR d\beta$ (or $2\pi\rho r^2 \sin\alpha g(r,\alpha) dr d\alpha$) represents the averaged number of O atoms found in the partial spherical shell with dR and $d\beta$ at distance R

and angle β (or with dr and $d\alpha$ at distance r and angle α) from one of the H atoms in the donor, where ρ is the molecular number density of the system. In contrast, for the acceptor definitions, the averaged number of H atoms in the partial spherical shell with dr and $d\gamma$ (or $d\psi$) at distance r and angle γ (or ψ) from the acceptor O at the origin is expressed as $2\pi\rho r^2 \sin\gamma g(r,\gamma) dr d\gamma \times 2$ (or $2\pi\rho r^2 \sin\psi g(r,\psi) dr d\psi \times 2$), where the factor of 2 arises due to the presence of two H atoms in one molecule. Note that $g(r,\psi)$ becomes ill-defined at $\psi = 0$ because that point is apparently singular due to $\sin\psi = 0$. The distribution function g results in the 2D PMF defined by $W = -k_{\mathrm{B}}T \ln g$, which plays a role of the free energy landscape of the H-bond.

We also analyze the time correlation function of the H-bond, $C(t) = \langle h(0)h(t)\rangle / \langle h(0)\rangle$, where $h(t)$ is the H-bond operator between any pair of water molecules at a time t [84,85]. $\langle \cdots \rangle$ represents the ensemble average over all the pairs of molecules at initial time 0. $h(t) = 1$ if the two water molecules are H-bonded and $h(t) = 0$ otherwise. The criterion of the H-bond was based on the 2D PMF for each definition, which will be discussed below. The H-bond lifetime τ_{HB} was determined from $C(t)$ by fitting it to the stretched exponential function $\exp(-t/\tau_{\mathrm{HB}})^{\beta}$.

3.3 Results and discussion

3.3.1 2D PMF profiles with donor definitions

We first discuss the results with the donor definitions, R-β and r-α. Figure 3.2 shows the 2D PMF contour maps using each distance-angle combination at $T = 300$ and 190 K. Remark that the overall 2D PMF profile remains unchanged at the temperatures investigated in this study.

The transition from the H-bonded to the non H-bond state is characterized by the saddle point on the 2D PMF profile. We detected the saddle points at $(R^*, \beta^*) = (0.32\ \mathrm{nm}, 39^\circ)$ and $(r^*, \alpha^*) = (0.25\ \mathrm{nm}, 52^\circ)$, which are indicated by gray dots in Fig. 3.2. These saddle point positions are also unchanged with the variation in the temperature.

(Reviewer 1, comment 1) We then fixed the H-bond criteria by identifying the energetically most stable regions on the 2D PMF profiles for the two definitions; two molecules are consid-

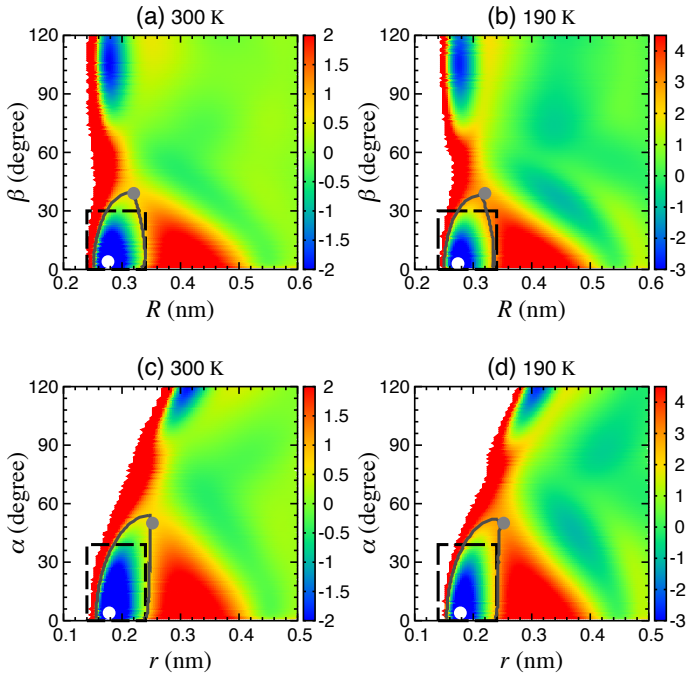

Figure 3.2: Contour plots of the 2D PMF, $W(R,\beta)$ at $T = 300$ (a) and 190 K (b), and $W(r,\alpha)$ at $T = 300$ (c) and 190 K (d). The value of W represented by the color scale is normalized by $k_{\mathrm{B}}T$. The global minimum and saddle points are shown by white and gray points, respectively. (Reviewer 1, comment 1) The gray line represents the equipotential contour line dividing the global minimum and the saddle point. The rectangle indicated by the black dashed line stands for the H-bond region. The region with unsampled configurations is depicted in white.

ered H-bonded if the distance-angle relationship are $(0.24\ \mathrm{nm}, 0^\circ) \leq (R,\beta) \leq (0.34\ \mathrm{nm}, 30^\circ)$ and $(0.14\ \mathrm{nm}, 0^\circ) \leq (r,\alpha) \leq (0.24\ \mathrm{nm}, 40^\circ)$. The present cut-off values are almost coincident with those reported in the previous study [64]. Note that the distances $R = 0.34$ nm and $r = 0.24$ nm correspond to the first minima of the radial distribution functions, $g_{\mathrm{OO}}(r)$ and $g_{\mathrm{OH}}(r)$, respectively. Rectangular areas indicated in Fig. 3.2 correspond to the H-bonded regions, resembling the energy-based dividing surfaces represented by the equipotential contour lines corresponding to the saddle points. Despite small differences between the two regions in terms of rectangular and equipotential lines, the energies of those configurations unshared by the two regions are much larger than those of global minimum points ($\gtrsim 3k_{\mathrm{B}}T$). Thus, such configurations are not likely to appear and the chosen cut-off values of the length and angle are appropriate for H-bond criteria.

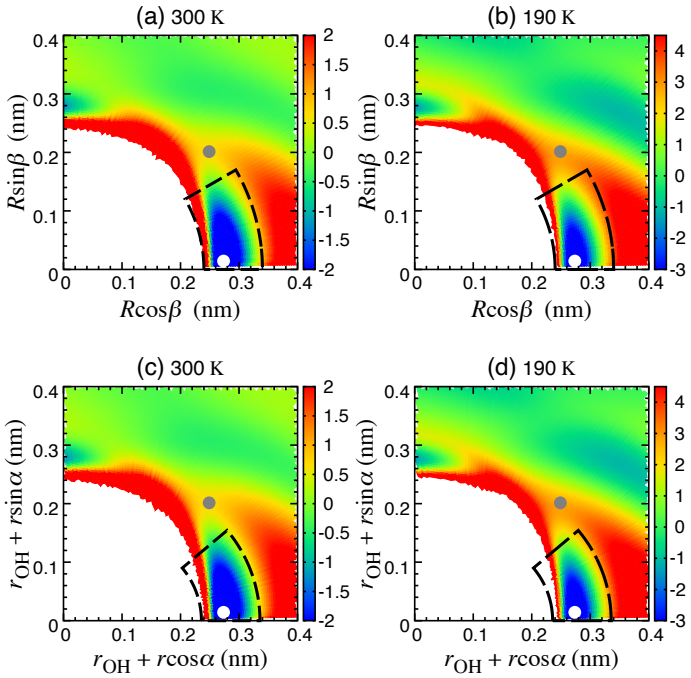

Figure 3.3: Contour plots of the 2D PMF, transformed $W(R,\beta)$ at $T = 300$ (a) and 190 K (b), and transformed $W(r,\alpha)$ at $T = 300$ (c) and 190 K (d). Note that the distance-angle combinations ($R\cos\beta$, $R\sin\beta$) [(a) and (b)] and ($r\cos\alpha + r_{\mathrm{OH}}$, $r\sin\alpha$) [(c) and (d)] are used, respectively (see also the orthogonal coordinates in Fig. 3.1(a)). The value of W represented by the color scale is normalized by $k_{\mathrm{B}}T$. The global minimum and saddle points are shown by white and gray points, respectively. The rectangle indicated by the black line stands for the H-bond region. The region with unsampled configurations is depicted in white.

For the R-β definition, the H-bond is expected to be broken mainly by increasing β. On the other hand, for the r-α definition, the pathway from the most stable state to the saddle point is accompanied by increases in the OH distance r and O-HO angle α. These saddle points indicate that the H-bond switching process utilizes the molecular reorientation, as described in various studies [68–71, 93]. Note that we have demonstrated that the pathways of H-bond breakages do not go through the saddle point, particularly in supercooled water [124]. In fact, we have observed that the H-bond breaks through traslational jump motions instead of the molecular reorientation, which are due to the collective, cage effect from neighboring molecules [125]. The 2D PMF profiles using only the distance-angle combinations between two molecules may not involve saddle points that are enough to characterize such collective motions.

The donor definitions of R-β and r-α consider the relative orientation of the OH bond of the donor and the O of the acceptor [64]. To examine the relationship between the two definitions, the geometrical variables are transformed from (R,β) and (r,α) into $(R\cos\beta, R\sin\beta)$ and $(r\cos\alpha + r_{\mathrm{OH}}, r\sin\alpha)$, respectively, where r_{OH} denotes the intramolecular OH bond distance. They are transformations to the orthogonal coordinates, as depicted in Fig. 3.1(a). The transformed 2D PMF profiles are displayed in Fig. 3.3. It is demonstrated that the two profiles from (R, β) and (r, α) are essentially identical to each other, having the almost same H-bond region on the orthogonal coordinates. This feature is observed at the other temperatures, too.

3.3.2 2D PMF profiles with acceptor definitions

Next, we examine the acceptor definitions, r-γ and r-ψ. Figure 3.4 shows the 2D PMF contour maps at $T = 300$ and 190 K. The overall behavior of the 2D PMF profile is not influenced by the temperature change, which is similar to the observations in Fig. 3.2.

The saddle point is found at $(r^*, \gamma^*) = (0.25\ \mathrm{nm}, 55^\circ)$ for the r-γ definition (see the gray points in Fig. 3.4(a) and (b)). In contrast, we cannot explicitly characterize a possible saddle point in the 2D PMF profile with r-ψ definition; that may be located around the apparent singular line of $\psi = 0$, below which the H-H repulsive interaction becomes dominant and causes H-bond break. Remark that the angle γ at the global minimum point with the acceptor definition moves from $\gamma = 38^\circ$ at 300 K to 52° at 190 K. The increase in the angle shows that the tetrahedral coordination is enhanced with decreasing the temperature. This corresponds to the fact that the structure of water is close to that of ice at supercooled conditions. In the ice structure forming a regular tetrahedron, $\gamma = 54.7^\circ$ since 2 donor molecules are symmetrical to the bisector of the acceptor molecule.

The O atom at the origin accepts two H-bonds from two neighboring molecules, particularly at lower temperatures. It should be noted that the coordinate transformation as done with respect to Fig. 3.3 is not possible with the acceptor definitions, r-γ and r-ψ. This is due to the fact that the angle axes are defined on different planes; γ is the angle from the ray of the bisector, while ψ is the angle from $\hat{z}$, as shown in Fig.3.1.

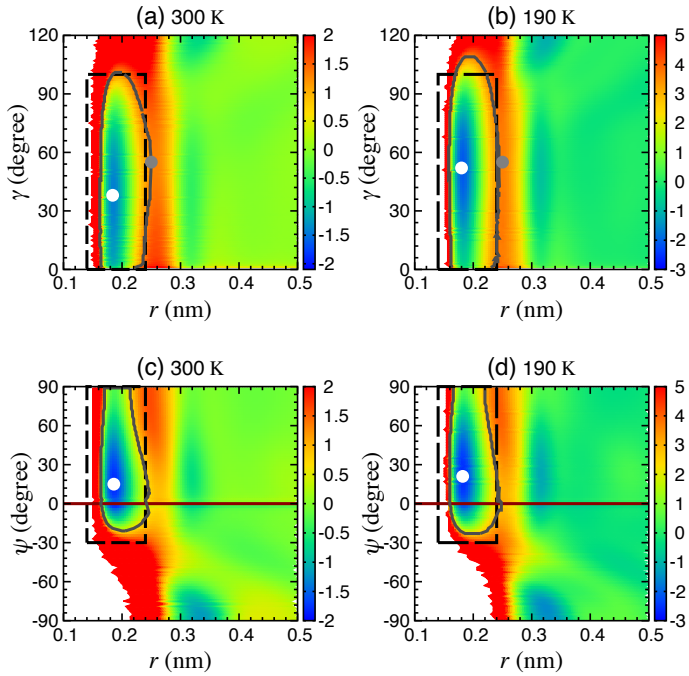

Figure 3.4: Contour plots of 2D PMF, $W(r,\gamma)$ at $T = 300$ K (a) and 190 K (b), and $W(r,\psi)$ at $T =$ 300 at $T = 300$ K (c) and 190 K (d). The value of W represented by the color scale is normalized by $k_{\mathrm{B}}T$. The global minimum and saddle points are shown by white and gray points, respectively. (Reviewer 1, comment 1) The gray line represents the equipotential contour line dividing the global minimum and the saddle point. Note that the gray contour in $r-\psi$ definition corresponds to $(r,\psi) = (0.24\ \mathrm{nm}, 1^\circ)$ instead of the singular point $\psi = 0$. The rectangle indicated by the black line stands for the H-bond region. The region with unsampled configurations is depicted in white. The horizontal lines in (c) and (d) show the apparent singular point $\psi = 0$ of $W(r,\psi)$.

We adopted geometrical criteria for the acceptor definitions for complementarity with those for the donor definitions. We determine the H-bond criteria from 2D PMF profiles as $(0.14\ \mathrm{nm}, 0^\circ) \leq (r,\gamma) \leq (0.24\ \mathrm{nm}, 100^\circ)$ and $(0.14\ \mathrm{nm}, -30^\circ) \leq (r,\psi) \leq (0.24\ \mathrm{nm}, 90^\circ)$, respectively. Rectangular areas in Fig. 3.4 indicate the H-bonded regions. As mentioned in Sec. 3.3.1, the distance $r = 0.24$ nm corresponds to the first minimum position of $g_{\mathrm{OH}}(r)$. As in the case of the donor definitions, the rectangle regions resemble the equipotential dividing surfaces, and thus the cut-off length and angle are appropriate for H-bond criteria. Note that the energy value for $r-\psi$ definition is chosen as that of $(r,\psi) = (0.24\ \mathrm{nm}, 1^\circ)$ instead of the singular point $\psi = 0$ in the acceptor definitions.

3.3.3 H-bond lifetime

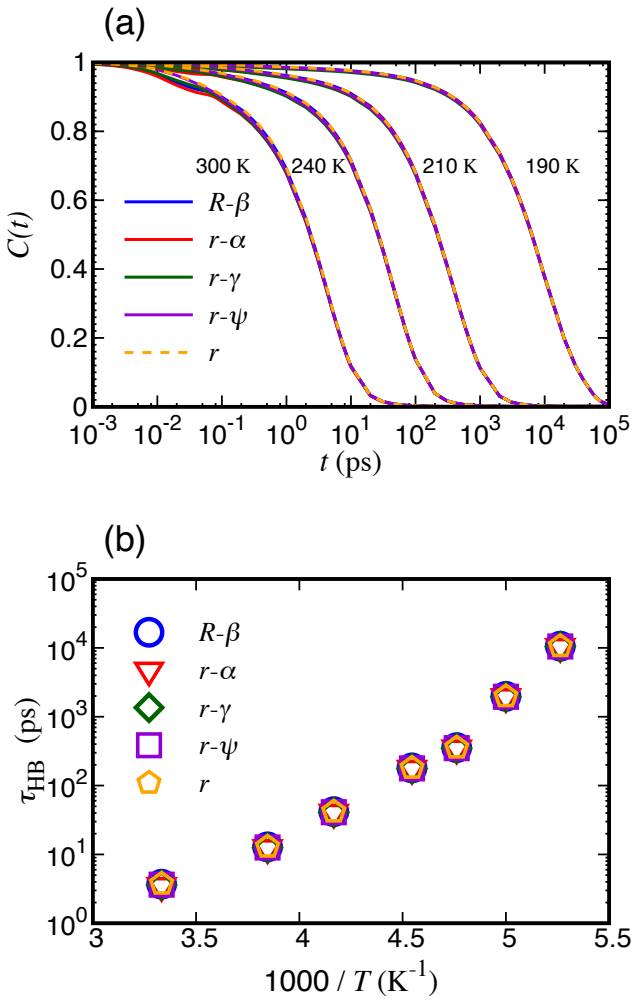

Figure 3.5: (a) H-bond correlation function $C(t)$ at $T = 300$, 240, 210, and 190 K from left to right. (b) H-bond lifetime τ_{HB} as a function of inverse temperature $1000/T$.

Finally, we examine the H-bond correlation function $C(t)$, from which the H-bond lifetime τ_{HB} was determined. The decay of $C(t)$ is plotted in Fig. 3.5(a) at $T = 300$, 240, 210, and 190 K. In comparison, we also show $C(t)$ in the r-definition, where only the distance r is used as the criterion of H-bond and two water molecules are H-bonded if the intermolecular OH distance is $r \leq 0.24$ nm [64]. Although the short time behavior of $C(t)$ is different among the H-bond definitions, the decay profiles are essentially coincident among one another Furthermore, the coincidence with

$C(t)$ in the r definition suggests that the H-bond breakage is accompanied with the increase in the intermolecular OH distance.

The H-bond lifetime τ_{HB} is plotted in Fig. 3.5 as a function of the inverse temperature. In all the definitions, τ_{HB} increases significantly with decreasing temperature. The temperature dependence of τ_{HB} is characterized by the Arrhenius equation, $\tau_{\mathrm{HB}} \propto \exp(E_{\mathrm{A}}/k_{\mathrm{B}}T)$ with the activation energy E_{A}. As shown in Fig. 3.5, E_{A} gradually increases with decreasing the temperature. The E_{A} was estimated in each definition as 27.4 and 51.5 kJ/mol at high and low temperatures, respectively, by fitting $\log(\tau_{\mathrm{HB}})$ to $1/T$ in $300 < T < 210$ K and $210 < T < 190$ K. Our results demonstrate that the H-bond lifetimes τ_{HB} obtained from the different definitions are consistent among one another even at supercooled states.

3.4 Conclusions

We analyzed H-bond breakage dynamics in the TIP4P/2005 supercooled water by using four geometric definitions of the H-bond. Two of the definitions set the coordinates with respect to the donor, and the other two are acceptor-based. We investigated the temperature dependence of the 2D PMF profiles determined with the four different distance-angle distribution functions. It was demonstrated in R-β, r-α, and r-γ definitions that the positions of the saddle points distinguishing the H-bond and non H-bond regions remain unchanged against the temperature variation from the ambient to supercooled. For the acceptor definitions of r-γ, we found that the angle γ of the global minimum point is influenced as the temperature is decreased. The H-bond correlation function $C(t)$ was calculated in the four H-bond definitions. While the profile of $C(t)$ is different at short times, the long-time decay of $C(t)$ is coincident among the different definitions. Correspondingly, the H-bond lifetime τ_{HB} is essentially the same over the examined range of temperature. Actually, it was found that the correlation function $C(t)$ and H-bond lifetime τ_{HB} do not change even when only the intermolecular OH distance is adopted as a one-dimensional coordinate to define the H-bond. The H-bond dynamics is thus insensitive to how the H-bond is characterized, which implies in turn

that a variety of computational and experimental studies involving different H-bond definitions in principle can be consistent among one another in practice.

Chapter 4

Diffusion dynamics of supercooled water modeled with the cage-jump motion and hydrogen-bond rearrangement

4.1 Introduction

The origin of slow dynamics observed in many supercooled liquids below their melting temperatures is frequently explained utilizing the cage-effect picture [26, 34]. This picture advocates that a molecule in supercooled liquids is trapped in the cage transiently formed by neighboring molecules and exhibits escape jump motions due to the cage-breaking after a sufficient long time. The cage-jump scenario also suggests intermittent molecular motions, which can be modeled by the continuous-time random walk using a random waiting time between cage-jumps [126]. The cage-jump motion in glassy dynamics has been extensively addressed with molecular dynamics (MD) simulations [29–31, 35, 118, 127–135] and experiments using colloidal glasses [32, 36, 37, 116, 136–139].

As the temperature is decreased, the mean square displacement (MSD) exhibits a plateau in the intermediate time scales between ballistic and diffusive regimes, reflecting the localized motion inside the cage. This MSD plateau value is associated with the the so-called Debye–Waller factor to characterize the degree of localization. However, it is often delicate to quantify the length and time scales of the cage effect from an MD trajectory, which is continuous in space and time and

is generated through thermal fluctuations. The cage-jump model adopts a discretized view and introduces the caged and jumping states along the dynamics of a single molecule.

Pastore *et al.* have recently developed a cage-jump model to predict the long-time diffusivity from the short-time cage dynamics in supercooled liquids [119, 120, 140–143]. In the study, a trajectory of a single particle is segmented into caged and jumping states. The segmentation criterion was given by the MSD plateau value. Remarkably, the evaluations of jumping length and duration time enabled to estimate the self-diffusion constant that is determined from the MSD long-time behavior at any temperature. This cage-jump modeling demonstrates that the underlying mechanism of the molecular diffusivity is essentially governed by the accumulation of successive cage-jump events.

The aim of this study is to develop a cage-jump model for supercooled water in strong connection to the dynamics of hydrogen-bond (H-bond) network. At normal liquid states, it has been widely accepted that a defect of 3- or 5-coordinated H-bond plays a crucial role for characterizing the H-bond breakage [68, 69, 93]. By contrast, the number of defects decreases when liquid water is supercooled. Correspondingly, the tetrahedrality of H-bond network becomes significant, where the molecular motion is expected to be described by the cage-jump scenario. Indeed, there have been various MD results showing the plateau in MSD of supercooled water [10, 11, 14, 18, 24, 33]. The intermittent jump motions have also been illustrated in supercooled water by analyzing the trajectory of a single molecule [33]. In particular, the connection of H-bond rearrangements with the jump motions has been examined.

We have recently revealed that the H-bond lifetime τ_{HB} depends on the temperature in inverse proportion to the self-diffusion constant D [24]. This result was explained by the correlation between H-bond breakages and translational molecular jumps. Moreover, we have also examined the pathways of H-bond breakages on the profile of the two-dimensional potential of mean force [124]. It has been clarified that H-bonds break due to translational, rather than rotational motions of the molecules, particularly at supercooled states. Although these studies suggest the strong relationship between the H-bond dynamics and molecular diffusivity in liquid water, the connection between

the microscopic change of the H-bond network and molecular displacement remains elusive.

The cage-jump model for supercooled water in the present work is established by analyzing the H-bond dynamics. In particular, the caged and jumping states are introduced from the rearrangement process of four-coordinated H-bonds. Thus, our cage-jump model does not rely on a dynamical criterion such as the MSD plateau value. We examine how the H-bond rearrangement process links to the long-time diffusivity.

4.2 Model and simulations

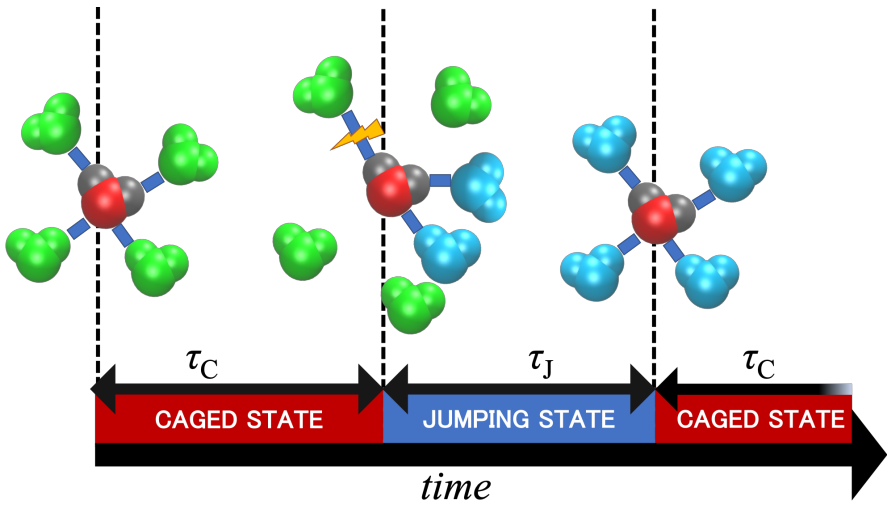

Figure 4.1: Schematic illustration to distinguish the caged (C) and jumping (J) states for a tagged water molecule (gray color). The tagged water molecule are H-bonded with neighboring four water molecules (green color), during which the state is labeled as a C state. At a certain point of time, all of four H-bonds are broken and the C state is switched to the J state. After a period of time, the tagged molecule are H-bonded with completely different four water molecules (cyan color), at which the state is switched to the next C state. The duration times of the J and C states are denoted as τ_J and τ_C, respectively.

MD simulations were performed using the TIP4P/2005 water model [144]. All the simulations in this work were performed with the GROMACS2016.4 package [110,111]. The phase diagram of

the TIP4P/2005 suerpcooled water was determined in Refs. [145, 146]. The temperature crossing the Widom line in the ρ-T phase diagram is $T_{\rm L} \approx 210$ K at 1 g/rm^3. Furthermore, the mode-coupling glass transition is estimated as $T_{\rm C} \approx 190$ K at 1 g/rm^3 in Refs. [20, 147]. Recent MD simulations have reported that the divergence of the structural relaxation time occurs at $T_{\rm g} \approx 136$ K under the constant 1 bar condition [4, 6]. As described next, we examined the systems close to $T_{\rm L}$, while our simulation temperatures are above $T_{\rm C}$ and $T_{\rm g}$.

The mass density was fixed at 1 g/cm^3 and the simulation system contained $N = 8,000$ molecules in a cubic box with the periodic boundary conditions. The cell length was approximately $L = 6.2$ nm. The investigated temperatures were $T =$ 350, 320, 300, 280, 260, 240, 220, 210, 200, and 190 K. At each temperature, the system was equilibrated for 10 ns in the NVT ensemble, followed by a production run in NVE for 20 ns. Other trajectories of 100 ns were generated for MSD and H-bond correlation function (see the definitions below) at temperatures 200 K and 190 K. A time step of 1 fs was used. As demonstrated below, this trajectory duration is larger than the H-bond lifetime $\tau_{\rm HB}$ at all the temperatures examined. Furthermore, aging effects have not been detected in the course of MD simulations. The atomic coordinates were stored at 0.2 ps intervals, which were used for the analyses presented below. This interval was chosen as a time scale slightly larger than that of libration motions (~ 0.1 ps).

The MSD, $\langle \delta r^2(t) \rangle = \langle \sum_{i=1}^{N} |\Delta \boldsymbol{r}_i(t)|^2 \rangle / N$, was calculated to quantify the self-diffusion constant D. Here, $\Delta \boldsymbol{r}_i(t)$ represents the displacement vector of an O atom of the molecule i between two times 0 and t. The results at various temperatures are shown in the inset of Fig. 4.4(b). At temperatures below 280 K, a plateau becomes noticeable during the intermediate times between ballistic and diffusive regimes, indicating the cage effect. The self-diffusion constant D was determined from the long-time behavior of the MSD, $D = \lim_{t\to\infty} \langle \delta r^2(t) \rangle / 6t$. The ratio of the Lennard–Jones diameter of TIP4P/2005 model and the unit cell is $\sigma/L \approx 0.05$, which is sufficiently small to eliminate the finite-size effect on the diffusion constant [148].

The H-bond was defined using geometric variables between two water molecules. We adopted O-O distance R and OH-O angle β [64]. Two water molecules are considered H-bonded if the

distance-angle relationship meets the condition, $(R, \beta) \leq (0.34\ \text{nm}, 30^\circ)$. The H-bond correlation function $c(t) = \langle h(0)h(t)\rangle / \langle h(0)\rangle$ was calculated with the H-bond indicator $h(t)$ at a time t [84,85]. It analyzes 'history-independent' H-bond correlations, in the sense that $h(t)$ is evaluated only from the configuration at time t without taking into account the reformation of the H-bond in the interval between times 0 and t. The H-bond lifetime τ_{HB} was then determined from $c(t)$ by fitting it to the stretched-exponential function $\exp[-(t/\tau_{\text{HB}})^{\beta}]$.

We classify the time course of each water molecule into two states. One is called caged (C) state, where the tagged water molecule is initially H-bonded to other four water molecules. The schematic illustration of the J and C states is given in Fig. 4.1. Since an H-bond is of finite lifetime, the four H-bonds with the tagged molecule are all broken at a certain time. This time is set to the start of the jumping (J) state. The next C state then begins at the formation of four H-bonds with water molecules that are totally different from those in the previous C state. The complete changes of the H-bond partners is the condition of transition from one C state to the next. The end time of a C state is when the four H-bonds are first broken, and the start time is when new, four bonds are formed. The adjacent C states are bridged by a J state, and by definition, a C state may be of 1, 2, 3 or 4 H-bonds and a J state may experience the reformation of an H-bond that was present in the previous C state. When an H-bond in the previous C state reforms after all the four bonds are once broken, the tagged molecule is still in the J state. The duration times of the C and J states are denoted as τ_{C} and τ_{J}, respectively. We also quantified the displacement vectors of the O atom of the molecule i during the J state, which is represented as $\Delta \boldsymbol{r}_i^{\text{J}}(\theta)$. Here, θ is the counter for molecule i to stay at J states from the initial time of the trajectory. Furthermore, many τ_{C} and τ_{J} were obtained for the single-molecule trajectory of each water molecule. The averages of τ_{C} and τ_{J} over all the single-molecule trajectories are denoted as $\langle \tau_{\text{C}} \rangle$ and $\langle \tau_{\text{J}} \rangle$, respectively. On the other hand, the sum of τ_{J} along a single trajectory was obtained and its ratio to the total length of that trajectory was also determined. The average of this ratio over all the single-molecule trajectories is then called ρ_{J}. Due to the difference in the order of averaging, ρ_{J} is in principle different from $\langle \tau_{\text{J}} \rangle / (\langle \tau_{\text{C}} \rangle + \langle \tau_{\text{J}} \rangle)$; this point will be examined at the end of Sec. 4.3. These quantities provide time coarse-grained

information filtering out the thermal fluctuations within the J states as well as the libration motions.

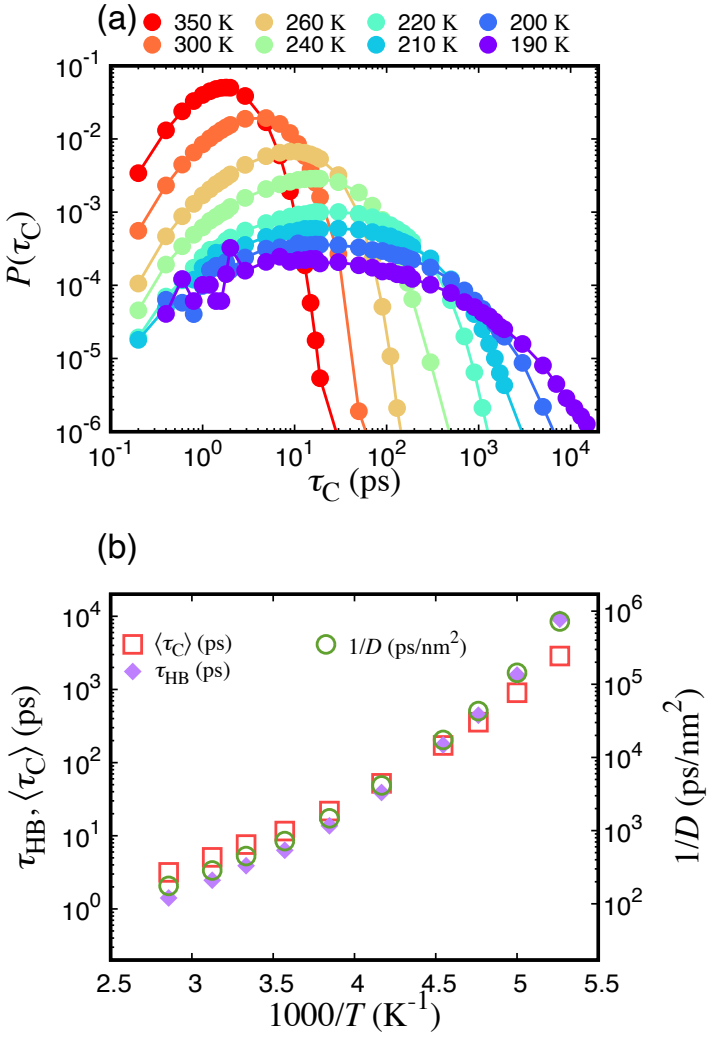

Figure 4.2: (a) Distribution of the duration time of the C state, $P(\tau_C)$, at the temperatures examined. (b) Average duration time $\langle\tau_C\rangle$ (left axis), H-bond lifetime τ_{HB} (left axis), and inverse of self-diffusion constant D^{-1} (right axis), as a function of the inverse of the temperature, $1000/T$.

4.3 Results and discussion

Figure 4.2(a) shows the distribution of the duration time of the C state, $P(\tau_C)$, at the temperatures examined. The peak of $P(\tau_C)$ appears at around 10 ps at 300 K, which shifts to time scale of 50 ps at

190 K. In addition, the distribution is gradually extended to slower time scales with decreasing the temperature. The temperature dependence of the average duration time $\langle \tau_C \rangle$ is plotted in Fig. 4.2(b). In comparison, the temperature dependence of τ_{HB} and D^{-1} is also plotted in Fig. 4.2(b). It is demonstrated that the time scales of $\langle \tau_C \rangle$ is akin to τ_{HB}, although the temperature dependence is slightly different. Note that the mean value of H-bond number depends on the temperature ranging from 3.62 at 300 K to 3.97 at 190 K, presumably resulting in the difference between $\langle \tau_C \rangle$ and τ_{HB}. Furthermore, the intimate connection between self-diffusion constant D and H-bond lifetime τ_{HB} is clarified in Fig. 4.2(b), which is equivalent to the previous demonstration, $D \propto {\tau_{HB}}^{-1}$, in TIP4P/2005 supercooled water [24]. The roles of $\langle \tau_C \rangle$ and τ_{HB} for the cage-jump model will be discussed later.

Figure 4.3(a) shows the distribution of the duration time of the J state, $P(\tau_J)$. Contrary to $P(\tau_C)$ in Fig. 4.2, the temperature dependence of $P(\tau_J)$ is much smaller. This causes the very weak temperature dependence of the average jumping time $\langle \tau_J \rangle \approx 1$ ps, as seen in the inset of Fig. 4.3(a). Figure 4.3(b) shows the distribution of the jumping length during the J state, $P(r_J)$ with $r_J = |\Delta \boldsymbol{r}_i^J|$. This demonstrates that the peak position length scale of $P(r_J)$ becomes smaller as the temperature is decreased. Furthermore, the exponential decay of $P(r_J)$ beyond the peak position is clearly observed at each temperature. Our results of $P(\tau_J)$ and $P(r_J)$ are compatible with those of supercooled liquid using simple potentials [140]. Note that these distributions $P(\tau_J)$ and $P(r_J)$ are sufficiently converged when plenty of jump events are accumulated, requiring times exceeding $\langle \tau_C \rangle$ and τ_{HB}.

We calculated the jumping mean square displacement (JMSD),

$$\langle \delta r_J^2(\Theta_J) \rangle = \frac{1}{N_J} \sum_{i=1}^{N_J} \sum_{\theta=1}^{\Theta_J} |\Delta \boldsymbol{r}_i^J(\theta)|^2, \tag{4.1}$$

where Θ_J is the total number of J states during an MD trajectory of a single water molecule. In addition, N_J denotes the number of molecules exhibiting Θ_J jumps in the course of the trajectory. Figure 4.4(a) shows that the JMSD $\langle \delta r_J^2(\Theta_J) \rangle$ is linear with Θ_J at each temperature. However, we

observed some deviations in the JMSD, particularly for larger Θ_J at lower temperatures (see the inset of Fig. 4.4(a)). These deviations from the linearity at large Θ_J are due to the fact that N_J becomes much smaller than N, leading to the insufficient ensemble average over the molecules. At 190 K, for example, N_J becomes smaller than N at $\Theta_J \gtrsim 10$. The average self-diffusion constant D_J of successive jumping events is determined from the relation, $D_J = \lim_{\Theta_J \to \infty} \langle \delta r_J^2(\Theta_J) \rangle / (\Theta_J \langle \tau_J \rangle)$, where the linear fit was done by excluding the $N_J < N$ regions. Figure 4.4(b) demonstrates that the second-order moment $\langle r_J^2 \rangle$ of the distribution $P(r_J)$ provides the good description of D_J at each temperature. As discussed in Ref [140]., these features of the JMSD and D_J indicate that the diffusion process of a single molecule can be described by the random walk with independent jumps, which is characterized by $\langle r_J^2 \rangle$. Furthermore, the decrease in D_J with the temperature reduction is attributed to the corresponding decrease in the jumping length scale $\langle r_J^2 \rangle$. The inset of Fig. 4.4(b) illustrates the location of $\langle r_J^2 \rangle$ in the MSD. At each temperature, the value of $\langle r_J^2 \rangle$ slightly exceeds beyond the MSD plateau. This observation indicates the validity of our modeling for cage-jump motions.

The relevance of the cage-jump modeling is examined in Fig. 4.5 by plotting the relationship between the self-diffusion constant D and $\rho_J D_J = \rho_J \langle r_J^2 \rangle / \langle \tau_J \rangle$. Note that the inset of Fig. 4.5 demonstrates the ratio of the J state ρ_J is essentially equal to the ratio of the average jumping time $\langle \tau_J \rangle / (\langle \tau_C \rangle + \langle \tau_J \rangle)$. A similar result was also reported in Ref [140].. It should be noted that ρ_J is obtained by first analyzing each single-molecule trajectory and then taking an average over all the single-molecule trajectories, while $\langle \tau_J \rangle$ and $\langle \tau_C \rangle$ are computed without distinguishing the trajectories of distinct water molecules. $\rho_J = \langle \tau_J \rangle / (\langle \tau_C \rangle + \langle \tau_J \rangle)$ thus implies the validity of a mean-field-type view in that the average over the single-molecule trajectories can be determined without taking into account the differences among the trajectories. Figure 4.5 shows that $\rho_J D_J$ from our cage-jump model is a good indicator for the self-diffusion constant D, although slight deviations are apparent at 190 K and higher temperatures above 300 K. As shown in Fig. 4.2(b), the inverse of the self-diffusion constant D^{-1} is strongly coupled with τ_{HB}, which becomes slightly larger than $\langle \tau_C \rangle$. When $\langle \tau_J \rangle \ll \langle \tau_C \rangle$, $\rho_J D_J$ is approximated by $\langle r_J^2 \rangle / \langle \tau_C \rangle$, which holds particularly at lower

temperatures. Thus, the difference between $\langle \tau_C \rangle$ and τ_{HB} results in the small difference between D and $\rho_J D_J$ at 190 K. The deviations at high temperatures are attributed to the observation that the MSD plateau was not well developed, as shown in the inset of Fig. 4.4(b). In fact, at higher temperatures, the cage structures are weakened and water molecules immediately diffuse without exhibiting intermittent cage-jump motions

4.4 Conclusions

In this paper, we have developed a cage-jump model for the diffusion in supercooled water. Unlike the scheme proposed by Pastore *et al.*, [119, 120, 140–143] we classify the trajectory of a single water molecule into the caged and jumping states from the analysis of H-bond rearrangements. The quantification of the average length and time scales of the jumping state enabled to predict the self-diffusion constant D that is determined in principle from the long-time MSD behavior. We have thus succeeded in connecting the H-bond dynamics and the molecular diffusivity through the cage-jump events. This cage-jump event can be regarded as an element of the collective motions, which are often visualized by string-like motions [33]. In fact, the time scale is $\langle \tau_J \rangle \approx 1$ ps, whereas that of collective motions is typically characterized by the time of the last stage in the MSD plateau.

Our cage-jump model gives an estimate of D when the caged and jumping states are identified from an MD trajectory, without extensive MSD evaluation to the diffusive regime. In fact, the diffusion asymptote $6Dt$ is observed at times much larger than τ_{HB}, as shown in the inset of Fig. 4.4(b). However, particularly at lower temperatures, the duration time of the C state $\langle \tau_C \rangle$ becomes slightly smaller than the H-bond lifetime τ_{HB}. This causes the small difference between D and $\rho_J D_J$, particularly at 190 K, as observed in Fig. 4.5. The local structure changes from high-density liquid to low-density liquid with decreasing the temperature below the so-called Widom line ($T_L \approx 210$ K). The tetrahedral order becomes higher and the number of the defect correspondingly decreases in the low-density liquid state, where the hydrogen-bond break needs more activation energy, and correspondingly the H-bond network rearranges over a wider range in space. In contrast, our cage-

jump model is constructed based on the information on the first nearest neighbor shell only. This leads to the underestimation of $\langle \tau_C \rangle$ compared with τ_{HB}. A possible refinement is thus to incorporate order parameters for H-bond network such as the local structure index [4, 149–152], which focus on the second nearest neighbor. In this respect, further study is currently undertaken toward the appropriate inference of the self-diffusion constant D, particularly at much deeper supercooled states inside the so-called no man's land region [2–6]. It is also worthy to apply our cage-jump model to various water models to give deeper insight into the role of the H-bond breakage on the molecular diffusivity in supercooled water.

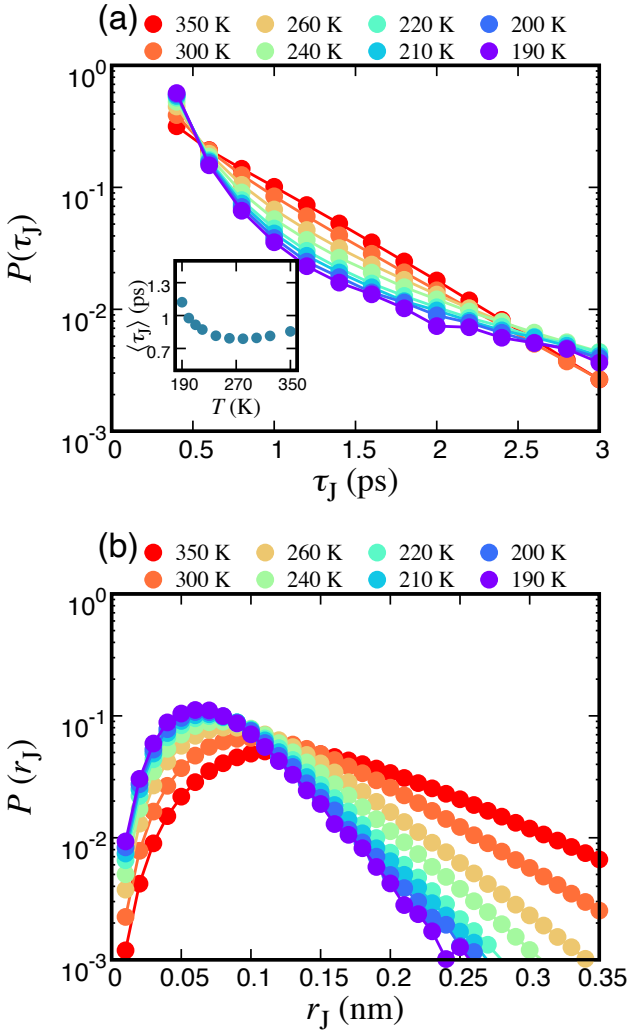

Figure 4.3: (a) Distribution of the duration time of the J state, $P(\tau_C)$, at the temperatures examined. Inset: temperature dependence of average jump time $\langle \tau_J \rangle$. (b) Distribution of the jumping length during the jumping state, $P(r_C)$, at the temperatures examined.

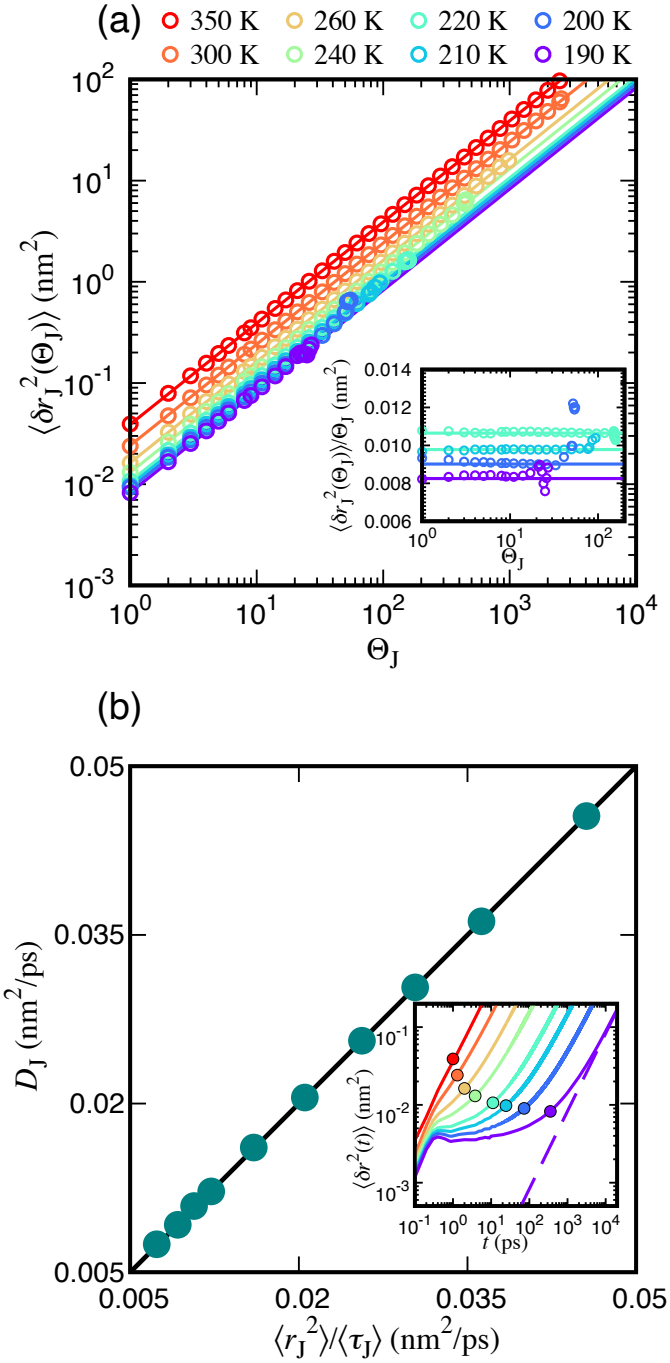

Figure 4.4: (a) Jumping mean square displacement (JMSD), $\langle \delta r_J^2(t) \rangle$, as a function of the number of jumps Θ_J at the temperatures examined. Inset: $\langle \delta r_J^2(t) \rangle / \Theta_J$ as a function of Θ_J at temperatures below $T = 200$ K. The straight lines indicate the diffusion behavior, of which slope gives a jumping self-diffusion constant D_J. (b) Jumping self-diffusion constant D_J vs. $\langle r_J^2 \rangle / \langle \tau_J \rangle$ obtained from $P(\tau_J)$ and $P(r_J)$. The black line represents $D_J = \langle r_J^2 \rangle / \langle \tau_J \rangle$. Inset: Mean square displacement (MSD), $\langle \delta r^2(t) \rangle$, at the temperatures examined. Dashed line represents the long-time asymptote $6Dt$ at $T = 190$ K. Points indicate values of the average jump length $\langle r_J^2 \rangle$ at each temperature.

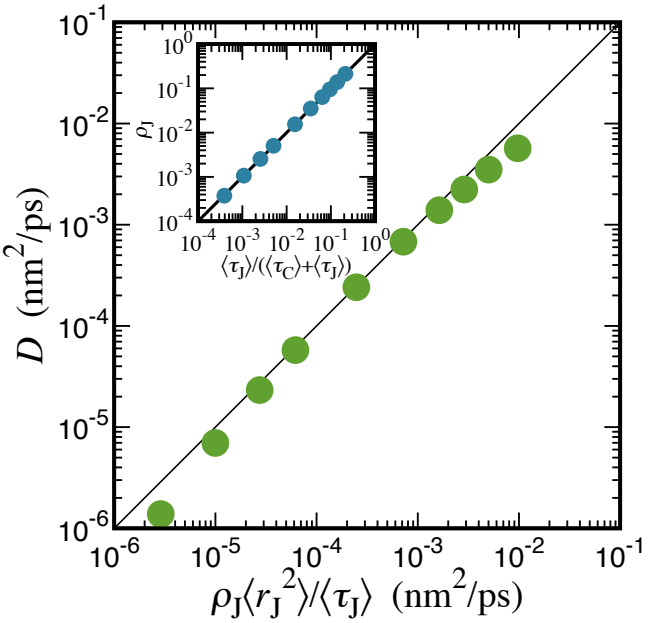

Figure 4.5: Self-diffusion constant D vs. the estimate from the cage-jump model $\rho_J\langle r_J^2\rangle/\langle\tau_J\rangle$. The black line represents $D = \rho_J\langle r_J^2\rangle/\langle\tau_J\rangle$. Inset: Ratio of jumping state ρ_J vs. the ratio of average jumping time $\langle\tau_J\rangle/(\langle\tau_C\rangle+\langle\tau_J\rangle)$. The black line represents $\rho_J = \langle\tau_J\rangle/(\langle\tau_C\rangle+\langle\tau_J\rangle)$.

Chapter 5

Transition pathway of hydrogen bond switching in supercooled water analyzed by the Markov state model

5.1 Introduction

Characterizing the hydrogen-bond (H-bond) dynamics is crucial for understanding various anomalies in liquid water using molecular dynamics (MD) simulations [73, 74, 92, 153–155]. A conventional method to analyze the H-bond dynamics employs the H-bond correlation function $c(t) = \langle h(t)h(0)\rangle / \langle h(t)\rangle$, where $h(t)$ denotes the H-bond operator At time t, $h(t) = 1$ if two water molecules are H-bonded, while $h(t) = 0$ in the absence of the H-bond [83–86]. The relaxation time of $c(t)$ corresponds to the average lifetime of a single H-bond. Various MD studies have characterized a collective motion, called "H-bond switching", to explain the molecular mechanism of the H-bond breaking and reforming [68–71]. Laage and Hynes demonstrated that an H atom of the donor molecule switches its H-bonded acceptor molecule to another molecule that was initially located in the second neighbor shell. The bifurcated H-bond structure was detected as the transition state, causing the reorientation of the donor molecule with a large angular jump [68, 69].

The dynamics exhibit a drastic slowing-down, particularly in supercooled water, similar to that observed in a variety of glass-forming liquids [2–4, 6, 10–20, 23, 25, 33, 41, 94, 122, 123, 156–160]. Correspondingly, the H-bond lifetime significantly increases with a decrease in the temperature

[22,24,66,79,90,93,161]. The clarification of the molecular mechanism of H-bond rearrangements when the liquid water undergoes supercooling is an area of interest. We recently examined the H-bond dynamics in supercooled water [124, 125, 162]. Specifically, the H-bond breakage pathway has been analyzed in terms of the two-dimensional (2D) potential of mean force (PMF), $W(R,\beta) = -k_{\mathrm{B}}T \ln g(R,\beta)$, with the Boltzmann constant k_{B} and a temperature T [124,162]. R and β represent the intermolecular O-O distance R and HO-O angle β, respectively, and $g(R,\beta)$ is the angular extension of the radial distribution function [64]. It was demonstrated that pathways not passing through the saddle point of the 2D PMF are evident in supercooled states. This observation suggests the need to examine more collective H-bond rearrangements beyond two-body correlations.

The Markov state model (MSM) is a computational tool that provides valuable information on the detailed molecular conformations of the transition pathway connecting reactant and product states [163]. The MSM is widely used for long-time MD simulations of various protein kinetics [164–171]. It has recently been demonstrated that the MSM is also applied to the investigation of solvent dynamics [172–174]. Hamm has reported the MD results showing the two-state behavior between high- and low-density liquids in supercooled water with the help of an MSM [173]. Furthermore, Schulz *et al.* have performed MSM analysis to study the collective H-bond switching in SPC/E water at room temperature [174]. They have quantified the mean first-passage time of the H-bond switching based on the MSM. In addition, they visualized the transition pathway network using the pathway decomposition method. The MSM characterized pathways via the intermediate state of the bifurcated H-bond structure proposed by Laage and Hynes and also picked up other sub-dominant pathways.

MSM analysis for the H-bond switching in supercooled water remains to be thoroughly studied. In the present work, we investigated it over a wide range of temperatures from the ambient to supercooled. The temperature dependence of the mean first-passage time associated with the H-bond switching was quantified, and was compared with the H-bond lifetime. In addition, we carried out the pathway decomposition, which revealed the individual transition pathways of the H-bond switching.

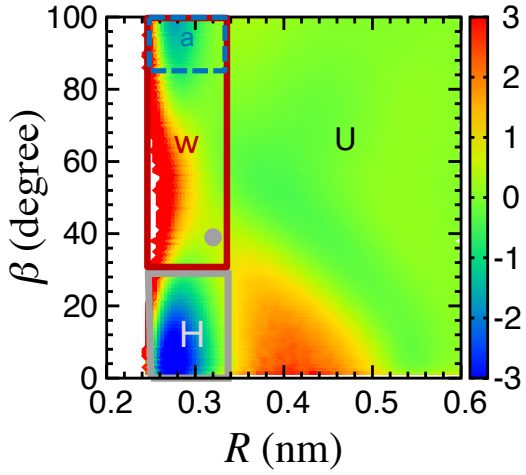

Figure 5.1: Contour plot of 2D PMF $W(R,\beta)/k_{\mathrm{B}}T$ at 300 K. The gray rectangular area represents "H" state ($R \leq 0.34$ nm and $\beta \leq 30^{\circ}$), the red area shows "w" state ($R \leq 0.34$ nm and $\beta > 30^{\circ}$), and "U" state is represented by the area not surrounded by any lines ($R > 0.34$ nm). The blue area roughly corresponds to "a" state, which cannot be strictly described on the 2D PMF (see the text in detail). The gray dot at $R \approx 0.32$ nm and $\beta \approx 40^{\circ}$ is the saddle point.

5.2 Methods

The TIP4P/2005 model was used for the liquid water [144]. In this model, the liquid-liquid critical point was found to be located at 182 K and 170 MPa in a deeply supercooled state [146]. MD simulations were carried out using the GROMACS2016.4 package [110, 111]. The simulation system contained $N = 1,000$ molecules in a cubic box with the periodic boundary conditions. The linear dimension of the box was 3.1 nm, and the corresponding mass density was 1 g/cm^3. The *NVT* ensemble was simulated at $T = 300$, 260, 240, 220, 210, 200, and 190 K for the equalibration, and trajectories were generated using the *NVE* ensemble for 100 ns at each temperature. A time step of 1 fs was employed.

We conducted MSM analysis for the switching of the H-bond acceptor, following a previous study by Schulz *et al.* [174]. As proposed in Ref [174]., the state of the water dimer was categorized into four basis states, "H", "w", "a", and "U". To clarify each state, we examined the distance-angle distribution function $g(R,\beta)$ with the intermolecular O-O distance R and HO-O angle β [64]. The contour plot of the 2D PMF $W(R,\beta) = -k_{\mathrm{B}}T \ln g(R,\beta)$ is shown in Fig. 5.1. The oxygen atom of

an tagged molecule is considered to be located at the origin of the coordinate, which is represented by O*. Furthermore, one hydrogen atom of the tagged molecule is placed on the horizontal axis of the plot, which is represented by H*. The temperature dependence of $W(R,\beta)$ was investigated in our previous studies, [124,162] where we concluded that the profile of $W(R,\beta)$ remains unchanged with decreasing the temperature.

Figure 5.1 depicts the four states on the 2D PMF plot. The H-bonded state, called "H", is defined as the region of $R \leq 0.34$ nm and $\beta \leq 30^\circ$. These threshold values are generally used to define the H-bond in MD simulations [84, 85]. Here, H* acts as the donor of the H-bond. The weakly H-bonded state, called "w", is defined as the region of $R \leq 0.34$ nm and $\beta > 30^\circ$. The molecule in the "w" state is located within the first nearest neighbor of the molecule at the origin, but H* and O are not H-bonded. Furthermore, the tagged water molecule at the origin is capable of H-bonding when either one of the following, two conditions is satisfied; (1) the hydrogen atom different from H* is H-bonded with the oxygen atom of an acceptor molecule. (2) O* is an acceptor of an H-bond and is H-bonded with the hydrogen atom of a donor molecule. We regard the molecules H-bonded with the tagged molecule as the alternative H-bonded state, referred to as "a". The intermolecular O*-O distance R fulfills $R < 0.34$ nm and the H*O*-O angle β typically exceeds 80°. This angle corresponds to the tetrahedral angle of 109.5° minus the amplitude of the angle of $\beta \approx 30^\circ$, providing the energetically stable state on the $W(R,\beta)$ plot, as shown in Fig. 5.1. However, the "a" state cannot be defined on the $W(R,\beta)$ plot and the region of $R \leq 0.34$ nm and $\beta > 80^\circ$ involve either the "w" or the "a" state. When a configuration of a pair of water molecules with $R \leq 0.34$ nm and $\beta > 80^\circ$ satisfies the conditions for "a", it is identified as "a" and as "w" otherwise. Finally, the unbounded state, called "U", is defined as the region of $R > 0.34$ nm regardless of the angle β.

The combination of these four states generates 4×4=16 states for three water molecules of one donor and two acceptors. Using those 16 states, we characterized the process of the H-bond switching: H^* was initially H-bonded with O^a and was not H-bonded with O^b, following which it formed an H-bond with O^b after breaking the H-bond with O^a. The state of O^a (O^b) changes "H"

to "U" ("U" to "H"), which can be represented by the HU→UH transition path using the 16 states composed of the four individual states.

For constructing the MSM matrix, we started recording trajectories when H^* and O^a are H-bonded and H^* and O^b are not H-bonded. After the acceptor switching between O^a and O^b, the recording was stopped if the H-bond between H^* and O^b is broken. This recording procedure is same as that demonstrated in Ref. [174]. We collected 1,000,000 configurations for three water molecules at each temperature, from which the MSM matrix (16×16) was generated. Furthermore, four basis states were classified based on the number of H-bonds in the acceptor molecule. That is, each basis state was further decomposed into three states, *i.e.*, three or fewer H-bonds, four H-bonds, and five or more H-bonds. For instance, "H" state was divided into H_3, H_4, and H_5. Thus, another MSM matrix (144×144) was analyzed.

5.3 Results and discussion

5.3.1 Lag time dependence of the implied time scale

For the MSM in M state space, the probability $\boldsymbol{p}(t)$ of the states at time t is propagated by the $M \times M$ transition probability matrix $\boldsymbol{T}(\tau)$:

$$\boldsymbol{p}(t+\tau) = \boldsymbol{p}(t)\boldsymbol{T}(\tau), \tag{5.1}$$

where τ represents the lag time and $M = 16$ for our treatments. The eigenvalues λ_i ($i = 1, 2, \cdots, M$) of $\boldsymbol{T}$ provide the information on relaxation time scales, called the i-th implied time scale t_i^*, in the MSM framework. The Markovian stochastic process requires the validity of the implied time scale t_i, which is independent of the lag time τ [163]. More specifically, the implied time scale t_i^* is defined from the eigenvalue λ_i of $\boldsymbol{T}$ as

$$t_i^* = -\frac{\tau}{\ln \lambda_i}, \tag{5.2}$$

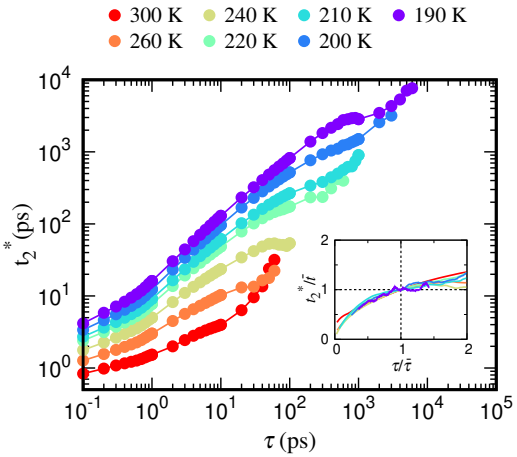

Figure 5.2: Implied time scale t_2^* for the second largest eigenvalue λ_2 as a function of lag time τ at the temperatures examined. Inset: the linear plot of $t_2^*/\bar{t}$ vs. $\tau/\bar{\tau}$ for all temperatures. Here, $\bar{\tau}$ represents the lag time in Table 5.1 and $\bar{t}$ is the corresponding implied timescale. The vertical and horizontal dotted lines denotes $\tau = \bar{\tau}$ and $t_2^* = \bar{t}$, respectively.

assuming $1 = \lambda_1 > \lambda_2 > \cdots > \lambda_M$. The largest eigenvalue $\lambda_1 = 1$ characterizes the stationary distribution of $\boldsymbol{T}$. Therefore, examining of the slowest implied time scale t_2^* for the second eigenvalue λ_2 as a function of τ is the test of the Markovian assumption.

Figure 5.2 shows the relationship between t_2^* and τ at each temperature. The time scale t_2^* increases with small lag times, where the time resolution is not appropriate for building the MSM. The implied time scale t_2^* reaches an approximate constant value with increasing the lag time τ, where $\boldsymbol{T}$ can be utilized as the Markov model. We fixed the minimal lag time $\bar{\tau}$ at each temperature, and the data are summarized in Table 5.1. It can be seen that $t_2^*/\bar{t}$, where $\bar{t}$ is t_2^* value at $\bar{\tau}$, is scaled by the $\tau/\bar{\tau}$ for all temperatures (see inset of Figure 5.2). In contrast, an issue pertaining to insufficient sampling occurs at lag times larger than the time scale of the Markovian assumption. Moreover, we investigated the relationship between τ and t_2^* for the 144×144 transition matrix (with further decomposition with respect to the number of H-bonds). The corresponding range of lag time τ with weakly varying t_2^* remained unchanged and the minimal lag times $\bar{\tau}$ were set to the values in Table 5.1 at all the temperatures.

Table 5.1: Lag time $\bar{\tau}$ of MSM analysis at examined temperatures.

T (K)	300	260	240	220	210	200	190
$\bar{\tau}$ (ps)	3	13	40	100	150	400	1400

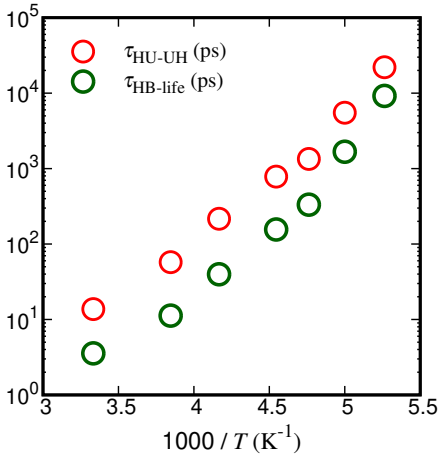

Figure 5.3: Mean first-passage time of H-bond switching $\tau_{\text{HU-UH}} = 1/k_{\text{HU}\to\text{UH}}$ and H-bond lifetime τ_{HB} as a function of the inverse of the temperature, $1000/T$.

5.3.2 Mean first-passage time of H-bond switching and H-bond lifetime

We examined the reaction rate of the HU→ UH transition path. In general, the reaction rate $k_{\text{A}\to\text{B}}$ is expressed by

$$k_{\text{A}\to\text{B}} = \frac{F}{\tau \sum_{i=1}^{M} \pi_i q_i}, \tag{5.3}$$

where F denotes the total flux of the transition path A→B, and π_i is the stationary probability of each state given by the MSM matrix $\boldsymbol{T}$, and q_i is the committor probability of each state [163, 165, 168]. The definitions of F and q_i and the calculation of $k_{\text{A}\to\text{B}}$ are briefly summarized in the Appendix 5.5. The mean first-passage time of the H-bond switching is correspondingly estimated by

$$\tau_{\text{HU-UH}} = 1/k_{\text{HU}\to\text{UH}}. \tag{5.4}$$

The temperature dependence of $\tau_{\text{HU-UH}}$ is shown in Figure 5.3. $\tau_{\text{HU-UH}} \approx 13$ ps at 300 K and is larger than that reported in a previous study using the SPC/E model (4.2 ps) [174]. The lag time τ

was fixed at 1 ps in Ref. [174], which is smaller than the 3 ps used in the present study. Generally speaking, a longer lag time leads to an increase in the mean first-passage time, owing to recrossing effects. We plotted the temperature dependence the H-bond lifetime $\tau_{\text{HB-life}}$, which is determined from the H-bond correlation function $c(t) = \langle h(0)h(t)\rangle / \langle h(0)\rangle$ with the H-bond operator $h(t) = 1$ in "H" state, or otherwise $h(t) = 0$ at time t [83–86]. $\langle \cdots \rangle$ represents the ensemble average over all the pairs of molecules at the initial time 0. The stretched exponential function, $\exp[-(t/\tau_{\text{HB-life}})^{\beta_{\text{HB}}}]$, was used for the fitting of $c(t)$ with the exponent $\beta_{\text{HB}} \approx 0.7$. Here $\tau_{\text{HB-life}}$ characterizes the average lifetime of a single H-bond. The two time scales $\tau_{\text{HU-UH}}$ and $\tau_{\text{HB-life}}$ exhibit similar temperature dependence, implying that the H-bond network change occurs in concert with the the acceptor switching event even in supercooled states. Notably, $\tau_{\text{HU-UH}}$ becomes slightly larger than $\tau_{\text{HB-life}}$ at any given temperature. This is because a single H-bond is likely to break before the H-bond switching is complete.

5.3.3 Temperature dependence of transition pathways of H-bond switching

The flux for the HU→UH transition pathway can be decomposed into independent pathways, characterizing the transition path network of H-bond switching [174]. The details of the pathway decomposition are explained in Refs. [163, 165, 168]. Here, we considered the direct pathway from HU to UH and the pathways connecting HU and UH through up to one intermediate state chosen from the 14 possible states. The accumulated flux was approximately 94% of the total flux at each temperature. This indicates that the pathways with two or more intermediate states play minor roles in the H-bond switching. Figure 5.4 shows the temperature dependence of a percentage of the six major individual pathways; HU→UH (direct transition), HU→no H-bond (ww, wU, Uw, or UU)→UH, HU→wH→UH, HU→Hw→UH, HU→aH→UH, and HU→Ha→UH.

We first found that the direct pathway of HU→UH without the intermediate state is the most dominant at any temperature, similar to Ref. [174]. The direct pathway is more prevalent than any other multi-step pathway. The second major pathway at 300 K passes through no H-bond state (ww, wU, Uw, or UU). Those states without H-bond account for the disordered structure apart from

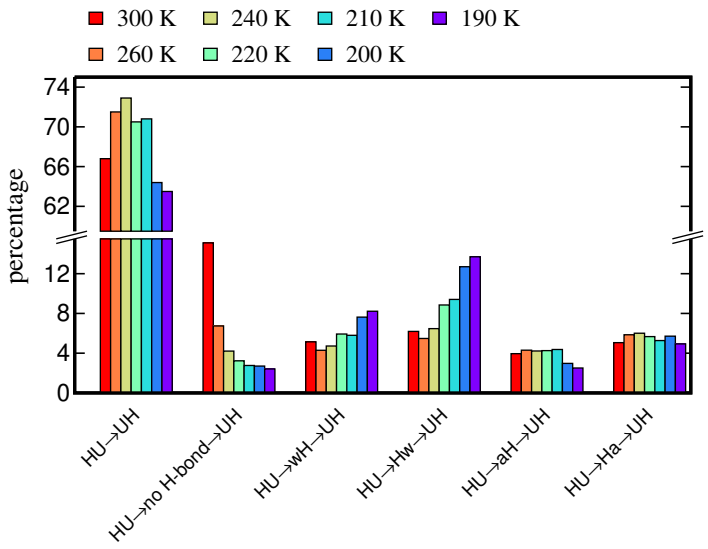

Figure 5.4: Temperature dependence of percentage of six dominant pathways, the direct transition HU→UH, HU→no H-bond (ww, wU, Uw, UU)→UH, HU→wH→UH, HU→Hw→UH, HU→aH→UH, and HU→Ha→UH.

the local tetrahedral structure. The population of these pathways decreased with decreasing temperature. Instead, the populations of HU→wH→UH and HU→Hw→UH increased in supercooled states, where the order of the tetrahedrality in H-bond network is increased. Note that "w" state includes the saddle point of the 2D PMF as a function of R and β (see Fig. 5.1). These two pathways indicate that the H-bond partner of the H^* atom switches between two different O^a and O^b atoms with a large reorientation of the donor molecule. The H-bond switching process using Hw or wH is consistent with the bifurcated H-bond structure, as demonstrated by Laage and Hynes [68, 69].

The second noticeable feature is the transition pathways through the "a" state, where the O* of the tagged molecule forms another H-bond with the H atom of O^a (or O^b) at the intermediate state of aH (or Ha). The total percentage of Ha and aH was approximately 10% at 300 K and exhibited a weak temperature dependence. The state "a" is not directly linked with the state "H", and the corresponding saddle point is not clearly manifested in the 2D PMF of $W(R,\beta)$. This indicates a more collective H-bond rearrangement. In fact, it has been demonstrated that the order of the locally

tetrahedral structure extends to the second neighbor shell in the supercooled water [3, 4, 50, 175]. In particular, the increase in the fraction of the locally tetrahedral structure is regarded as a sign of the crossover from high-density to low-density structure. The transition pathways through Ha and aH proceed by utilizing the tetrahedral structure, according to the definition of the "a" state. Thus, it is important to decompose 16 states into 144 states based on the H-bond number of the acceptor molecule.

5.3.4 Further decomposition based on the H-bond number of acceptor

To characterize the sub-dominant transition pathways through the state "a", the intermediate states, Ha and aH, are further decomposed into nine states based on the H-bond number of the acceptor molecule, the details of which are explained in Sec. 5.2. Figure 5.5 shows the decomposition results of the intermediate states Ha (a) and aH (b). The transition probabilities through states including H-bond defects, *i.e.*, three or five state, decrease with decreasing temperature. This behavior is in accordance with the fact that each molecule up to the second neighbor shell of a central water molecule tends to have four H-bonds in the supercooled state. In contrast, the transition probabilities through H_4a_4 and a_4H_4 increase as the temperature is decreased, indicating that acceptor switching occurs by utilizing the tetrahedral network rearrangement, instead of H-bond defects. Such competition between the decrease in H-bond defects and the increase in the degree of the tetrahedrality up to the second neighbor shell of the donor molecule leads to the weak temperature dependence of the transition pathways through Ha and aH, as demonstrated in Fig. 5.4. The percentages of the transition pathways HU$\rightarrow a_4H_4\rightarrow$UH peak at 210 K and subsequently decrease below this temperature. The timing of the H-bond breakage is different between the two pathways with the intermediate state "a"; one H-bond between H^* and O^a must be broken to form the aH state, following which another H-bond of the molecule belonging to O^a is then broken after aH. Alternatively, two H-bonds of the molecule belonging to O^* are broken after the Ha state. This difference in the pathway presumably causes the decreased percentage of HU$\rightarrow a_4H_4\rightarrow$UH in a highly supercooled state.

5.4 Conclusions

In this study, we examined the H-bond switching events in supercooled water using MSM analysis. Four basis states, "H", "w", "a", and "U", were defined for two water molecules and examined based on the 2D PMF $W(R,\beta)$ using O*-O distances R and H*O*-O angle β. The configuration of the three water molecules was then characterized by 4×4 states. A 16×16 transition probability matrix was constructed and diagonalized. By analyzing the largest implied time scale t_2^* as a function of the lag time τ, we determined the appropriate lag time for the Markovian process, which increases rapidly with decreasing temperature. According to the MSM framework, we estimated the reaction rate of the transition path HU→UH, which characterizes the mean first-passage time $\tau_{\mathrm{HU-UH}}$ of the acceptor switching. We showed that $\tau_{\mathrm{HU-UH}}$ exhibits a temperature dependence similar to that of the H-bond lifetime $\tau_{\text{HB-life}}$ from the H-bond correlation function.

Furthermore, we performed the pathway decomposition for the HU→UH transition. It was found that the main contribution was the direct pathway without an intermediate state. The next dominant pathway was through no H-bond states at 300 K. These features are consistent with those obtained in a previous study [174]. However, the pathways through no H-bond states play a minor role in supercooled states because of the increase in the ordered structure. Contrarily, the transition pathways involving the weakly H-bond state "w" become noticeable with decreasing the temperature. In addition, we found that the population of other pathways through the alternative H-bond state "a" exhibits weak temperature dependence. To clarify the pathways of HU→aH→UH and HU→Ha→UH in detail, we further decomposed 16 basis states into 144 states based on the number of H-bonds of the acceptor molecules. It was demonstrated that the pathways via the state "a" are picked-up when the degree of the four-coordinated H-bond structure becomes large, particularly in supercooled states. This peculiar pathway can be characterized by using the information on the second neighbor shell of the donor molecule, further elucidating the H-bond rearrangement process in supercooled water. The investigation of transition pathways of H-bond switching in a wider range of phase diagram can be important to clarify the liquid-liquid transition in supercooled

water, which is left for future work.

5.5 Appendix :Committer probability and reaction rate

For the transition path analysis, the committer probability q_i^{B} is the probability when being at an intermediate stable point i, the system will reach the product state B rather than the reactant state A [163, 165, 168]. According to the detailed balance, the forward and backward committer probabilities satisfy the condition:

$$q_i^{\mathrm{B}} + q_i^{\mathrm{A}} = 1. \tag{5.5}$$

Furthermore, if $i \in \mathrm{A}$, q_i^{B} is 0, and if $i \in \mathrm{B}$, $q_i^{\mathrm{B}} = 1$, by definition. The committer probability for all intermediate states is obtained by solving the following equation:

$$-q_i^{\mathrm{B}} + \sum_{k \in I} T_{ik} q_k^{\mathrm{B}} = -\sum_{k \in \mathrm{B}} T_{ik}, \tag{5.6}$$

where T_{ik} is the transition probability from state i to k, and I denotes the intermediate subset that includes all parts except for A and B. The committer q_i^{B} approaches 1 when the state i is close to B depart from A. Furthermore, the flux f_{ij} from i to j is defined by

$$f_{ij} = \pi_i q_i^A T_{ij} q_j^B, \tag{5.7}$$

where only reactive trajectories from A to B only are considered. The total flux F leaving from A is given by

$$F = \sum_{i \in \mathrm{A}} \sum_{j \notin \mathrm{A}} f_{ij} = \sum_{i \in \mathrm{A}} \sum_{j \notin \mathrm{A}} \pi_i T_{ij} q_j^{\mathrm{B}}, \tag{5.8}$$

which must be equal to the total flux entering B. Finally, the reaction rate k_{AB} from $A \to B$ is estimated by

$$k_{\mathrm{A}\to\mathrm{B}} = \frac{F}{\tau \sum_{i=1}^{M} \pi_i q_i^{\mathrm{A}}}, \tag{5.9}$$

where τ is the lag time of the transition matrix $\boldsymbol{T}$. Correspondingly, the mean first-passage time is given by

$$\tau_{\mathrm{mfp}} = 1/k_{\mathrm{A}\to\mathrm{B}}. \tag{5.10}$$

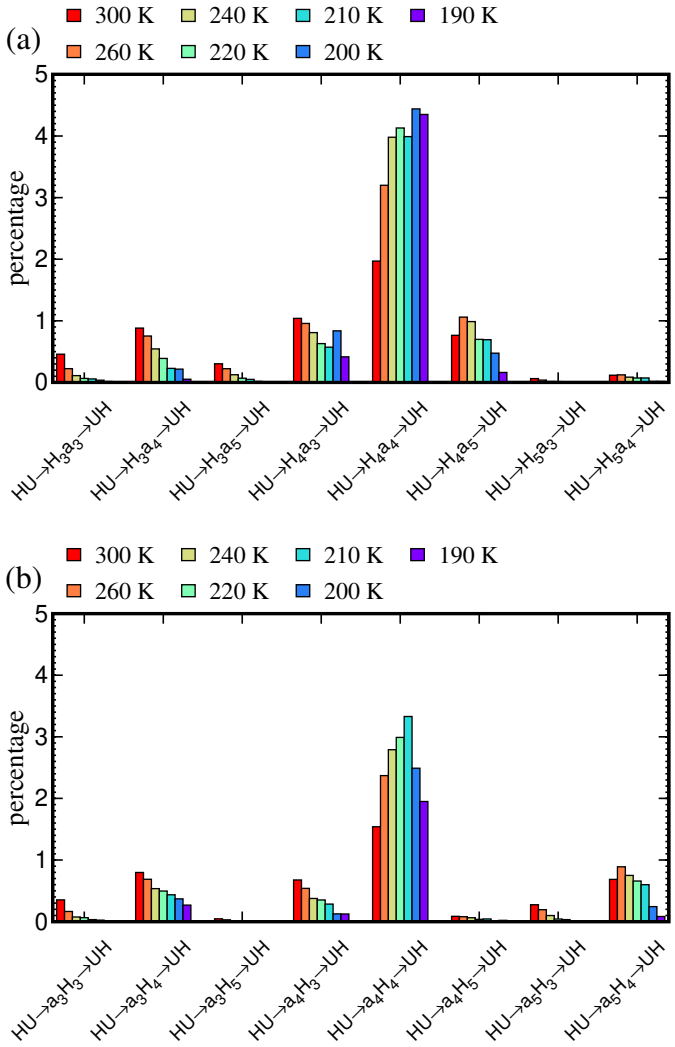

Figure 5.5: Temperature dependence of detailed transition probabilities for (a) Ha and (b) aH. The subscript number represents the number of H-bond on the acceptor molecule.

Chapter 6

General Conclusion

We analyzed the relationship between the structure and dynamics of the H-bonds in supercooled water. The following conclusions were obtained:

Chapters 2 and 3 show that the H-bond lifetime rapidly increases with the cooling of supercooled water with different breakage pathways at room temperature. The H-bond lifetime increased exponentially and had different activation energies after 240 K, and the same result was obtained for any geometric structure between the molecules. No 2D-PMF based on two-body water molecule variables satisfies the transition state theory and cannot represent the H-bond breaking of supercooled water. The 2D-PMF maps discussed in these chapters adequately represent the H-bond breakage pathway with an amplitude angular jump at room temperature. This indicates that the process of H-bond breakage in supercooled water may differ from that in ambient water by at least a three-body structural change in supercooled water.

Chapter 4 improved the cage-jump method using H-bond network rearrangement. With this research, we connect the short-term dynamics of local structural change with the long-term dynamics for the entire system. This result also suggests that H-bond breakage dominates diffusive motion, and that the temperature dependence of the H-bond lifetime is coupled with that of the diffusion coefficient. This study also provides direct insight into the impact of short-term dynamic heterogeneity on diffusivity reduction. On the other hand, this study classifies cage-jump states by the dynamics of H-bond networks, but not by the structure of static H-bond networks. This is probably because the network structure beyond the second neighbor shell is related to the breaking of a single H-bond, as discussed in Chapter 5. As the motion of water molecules is dominated

by hydrogen bonds, breaking the surrounding hydrogen bonds is necessary for jump mutations. Therefore, it is necessary to include molecular information such as the network structure in the second coordination sphere in the analysis.

In Chapter 5, H-bond switching events are investigated using the Markov state model. First, four basis states for the water dimer were set using the intermolecular distance and angle introduced in Section 2. It was found that the first mean passage time of H-bond switching events given by the Markov state model increases exponentially with supercooling, similar to the H-bond lifetime. Path decomposition analysis confirmed that the H-bond switching motion proceeding without forming an intermediate state was dominant at all the examined temperatures. Next, the four basis states were further divided into 12 states based on the number of H-bonds bonded to an acceptor molecule, and an MSM matrix was built. It was found that a system without defective states in the hydrogen bond network is easier to adopt when the acceptor molecule switches to the supercooled state. In the absence of H-bond network defects, H-bond acceptor switching is predicted to require more time because it requires more activation energy than the pathway with the H-bond network. The process without the H-bond network defects extends the lifetime of the H-bond in the supercooled state, indicating that it is a unique breakage process in the supercooled state.

Throughout, the relationship between the temperature dependence of H-bond dynamics, intermolecular structural changes, effect on the mobility of the entire system, and collective motion of H-bond networks extending into the second neighbor was clarified. The network becomes so strong that it undergoes a change in the entire network structure to break a single H-bond, dramatically increasing the H-bond lifetime. In addition, the diffusivity of molecules is controlled by H-bond breakage because the H-bond networks surround the molecules as a cage. We used various models to evaluate the dynamics but have yet to identify the collective variable that causes hydrogen bond breaking. If this structure could be identified, the transition state theory used in Chapter 2 would be valid, and the rate of existence in the system would determine the classification in Chapter 3. Identifying such collective variables is necessary for a comprehensive understanding of all models and will be investigated in the future.

References

[1] D. Eisenberg, W. Kauzmann, The structure and properties of Water, Oxford University Press, 2005.

[2] R. Shi, J. Russo, H. Tanaka, Origin of the emergent fragile-to-strong transition in supercooled water, Proc. Natl. Acad. Sci. U.S.A. 115 (38) (2018) 9444–9449.

[3] R. Shi, J. Russo, H. Tanaka, Common microscopic structural origin for water's thermodynamic and dynamic anomalies, J. Chem. Phys. 149 (22) (2018) 224502.

[4] S. Saito, B. Bagchi, I. Ohmine, Crucial role of fragmented and isolated defects in persistent relaxation of deeply supercooled water, J. Chem. Phys. 149 (12) (2018) 124504.

[5] Y. Ni, N. J. Hestand, J. L. Skinner, Communication: Diffusion constant in supercooled water as the Widom line is crossed in no man's land, J. Chem. Phys. 148 (19) (2018) 191102.

[6] S. Saito, B. Bagchi, Thermodynamic picture of vitrification of water through complex specific heat and entropy: A journey through "no man's land", J. Chem. Phys. 150 (5) (2019) 054502.

[7] O. Mishima, L. Calvert, E. Whalley, An apparently first-order transition between two amorphous phases of ice induced by pressure, Nature 314 (6006) (1985) 76–78.

[8] O. Mishima, Reversible first-order transition between two h2o amorphs at 0.2 gpa and 135 k, The Journal of chemical physics 100 (8) (1994) 5910–5912.

[9] P. H. Poole, F. Sciortino, U. Essmann, H. E. Stanley, Phase behaviour of metastable water, Nature 360 (6402) (1992) 324–328.

[10] P. Gallo, F. Sciortino, P. Tartaglia, S. H. Chen, Slow Dynamics of Water Molecules in Supercooled States, Phys. Rev. Lett. 76 (15) (1996) 2730–2733.

[11] F. Sciortino, P. Gallo, P. Tartaglia, S. H. Chen, Supercooled water and the kinetic glass transition, Phys. Rev. E 54 (6) (1996) 6331–6343.

[12] F. Sciortino, L. Fabbian, S. Chen, P. Tartaglia, Supercooled water and the kinetic glass transition. II. Collective dynamics, Phys. Rev. E 56 (1997) 5397–5404.

[13] N. Giovambattista, S. Buldyrev, F. Starr, H. Stanley, Connection between Adam-Gibbs Theory and Spatially Heterogeneous Dynamics, Phys. Rev. Lett. 90 (2003) 085506.

[14] N. Giovambattista, S. Buldyrev, H. Stanley, F. W. Starr, Clusters of mobile molecules in supercooled water, Phys. Rev. E 72 (1) (2005) 011202.

[15] S. Chen, F. Mallamace, C. Mou, M. Broccio, C. Corsaro, A. Faraone, L. Liu, The violation of the Stokes-Einstein relation in supercooled water., Proc. Natl. Acad. Sci. U.S.A. 103 (35) (2006) 12974–12978.

[16] P. Kumar, S. Buldyrev, S. R. Becker, P. Poole, F. Starr, H. Stanley, Relation between the Widom line and the breakdown of the Stokes–Einstein relation in supercooled water, Proc. Natl. Acad. Sci. U.S.A. 104 (23) (2007) 9575–9579.

[17] L. Xu, F. Mallamace, Z. Yan, F. Starr, S. Buldyrev, H. E Stanley, Appearance of a fractional Stokes-Einstein relation in water and a structural interpretation of its onset, Nat. Phys. 5 (2009) 565–569.

[18] P. Gallo, M. Rovere, Mode coupling and fragile to strong transition in supercooled TIP4P water, J. Chem. Phys. 137 (16) (2012) 164503.

[19] A. Dehaoui, B. Issenmann, F. Caupin, Viscosity of deeply supercooled water and its coupling to molecular diffusion, Proc. Natl. Acad. Sci. U.S.A. 112 (39) (2015) 12020–12025.

[20] M. De Marzio, G. Camisasca, M. Rovere, P. Gallo, Mode coupling theory and fragile to strong transition in supercooled TIP4P/2005 water, J. Chem. Phys. 144 (7) (2016) 074503.

[21] E. Guillaud, S. Merabia, D. de Ligny, L. Joly, Decoupling of viscosity and relaxation processes in supercooled water: a molecular dynamics study with the TIP4P/2005f model, Phys. Chem. Chem. Phys. 19 (3) (2017) 2124–2130.

[22] N. Galamba, On the hydrogen-bond network and the non-Arrhenius transport properties of water., J. Phys.: Condens. Matter 29 (1) (2017) 015101.

[23] M. De Marzio, G. Camisasca, M. Rovere, P. Gallo, Fragile to strong crossover and Widom line in supercooled water: A comparative study, Front. Phys. 13 (1) (2017) 7463.

[24] T. Kawasaki, K. Kim, Identifying time scales for violation/preservation of Stokes-Einstein relation in supercooled water, Sci. Adv. 3 (8) (2017) e1700399.

[25] L. Singh, B. Issenmann, F. Caupin, Pressure dependence of viscosity in supercooled water and a unified approach for thermodynamic and dynamic anomalies of Water, Proc. Natl. Acad. Sci. U.S.A. 114 (17) (2017) 4312–4317.

[26] C. A. Angell, Formation of Glasses from Liquids and Biopolymers, Science 267 (1995) 1924–1935.

[27] H. Vogel, The law of the relation between the viscosity of liquids and the temperature, Phys. Z 22 (1) (1921) 645–646.

[28] W. Hesse, G. Tammann, Dependence of viscosity on the temperature of su-ercooled liquids, Anorg. Allgem. Chem. 156 (1926) 245–257.

[29] R. Yamamoto, A. Onuki, Dynamics of highly supercooled liquids: Heterogeneity, rheology, and diffusion, Phys. Rev. E 58 (3) (1998) 3515–3529.

[30] M. M. Hurley, P. Harrowell, Kinetic structure of a two-dimensional liquid, Phys. Rev. E 52 (2) (1995) 1694–1698.

[31] R. Candelier, A. W. Cooper, J. K. Kummerfeld, O. Dauchot, G. Biroli, P. Harrowell, D. R. Reichman, Spatiotemporal Hierarchy of Relaxation Events, Dynamical Heterogeneities, and Structural Reorganization in a Supercooled Liquid, Phys. Rev. Lett. 105 (2010) 135702.

[32] W. K. Kegel, A. van Blaaderen, Direct Observation of Dynamical Heterogeneities in Colloidal Hard-Sphere Suspensions, Science 287 (2000) 290–293.

[33] N. Giovambattista, M. G. Mazza, S. Buldyrev, F. Starr, H. Stanley, Dynamic Heterogeneities in Supercooled Water, J. Phys. Chem. B 108 (21) (2004) 6655–6662.

[34] W. Gotze, Recent tests of the mode-coupling theory for glassy dynamics, J. Phys.: Condens. Matter 11 (10A) (1999) A1–A45.

[35] B. Doliwa, A. Heuer, Cage Effect, Local Anisotropies, and Dynamic Heterogeneities at the Glass Transition: A Computer Study of Hard Spheres, Phys. Rev. Lett. 80 (1998) 4915.

[36] P. N. Pusey, W. van Megen, Observation of a glass transition in suspensions of spherical colloidal particles, Phys. Rev. Lett. 59 (18) (1987) 2083–2086.

[37] A. Kasper, E. Bartsch, H. Sillescu, Self-Diffusion in Concentrated Colloid Suspensions Studied by Digital Video Microscopy of Core − Shell Tracer Particles, Langmuir 14 (18) (1998) 5004–5010.

[38] P. G. Debenedetti, Supercooled and glassy water, J. Phys.: Condens. Matter 15 (45) (2003) R1669–R1726.

[39] H. E. Stanley (Ed.), Liquid Polymorphism, Vol. 152 of Adv. Chme. Phys., J. Wiley & Sons, Inc., Hoboken, NJ, USA, 2013.

[40] P. Gallo, K. Amann-Winkel, C. A. Angell, M. A. Anisimov, F. Caupin, C. Chakravarty, E. Lascaris, T. Loerting, A. Z. Panagiotopoulos, J. Russo, J. A. Sellberg, H. E. Stanley, H. Tanaka, C. Vega, L. Xu, L. G. M. Pettersson, Water: A Tale of Two Liquids., Chem. Rev. 116 (13) (2016) 7463–7500.

[41] R. Shi, H. Tanaka, The anomalies and criticality of liquid water, Proc. Natl. Acad. Sci. U.S.A. (Oct. 2020).

[42] J. C. Palmer, F. Martelli, Y. Liu, R. Car, A. Z. Panagiotopoulos, P. G. Debenedetti, Metastable liquid–liquid transition in a molecular model of water, Nature 510 (7505) (2014) 385–388.

[43] O. Mishima, H. E. Stanley, The relationship between liquid, supercooled and glassy water, Nature 396 (6709) (1998) 329–335.

[44] N. J. Hestand, J. Skinner, Perspective: Crossing the widom line in no man's land: Experiments, simulations, and the location of the liquid-liquid critical point in supercooled water, The Journal of chemical physics 149 (14) (2018) 140901.

[45] P.-L. Chau, A. Hardwick, A new order parameter for tetrahedral configurations, Molecular Physics 93 (3) (1998) 511–518.

[46] J. R. Errington, P. G. Debenedetti, Relationship between structural order and the anomalies of liquid water, Nature 409 (6818) (2001) 318–321.

[47] A. K. Soper, M. A. Ricci, Structures of high-density and low-density water, Physical review letters 84 (13) (2000) 2881.

[48] Z. Yan, S. V. Buldyrev, P. Kumar, N. Giovambattista, P. G. Debenedetti, H. E. Stanley, Structure of the first-and second-neighbor shells of simulated water: Quantitative relation to translational and orientational order, Physical Review E 76 (5) (2007) 051201.

[49] M. J. Cuthbertson, P. H. Poole, Mixturelike behavior near a liquid-liquid phase transition in simulations of supercooled water, Physical review letters 106 (11) (2011) 115706.

[50] J. Russo, H. Tanaka, Understanding water's anomalies with locally favoured structures, Nat. Commun. 5 (2014) 3556.

[51] E. Shiratani, M. Sasai, Molecular scale precursor of the liquid–liquid phase transition of water, The Journal of chemical physics 108 (8) (1998) 3264–3276.

[52] R. Shi, H. Tanaka, Microscopic structural descriptor of liquid water, The Journal of Chemical Physics 148 (12) (2018) 124503. arXiv:https://doi.org/10.1063/1.5024565, doi:10.1063/1.5024565.
URL https://doi.org/10.1063/1.5024565

[53] R. Shi, H. Tanaka, Direct evidence in the scattering function for the coexistence of two types of local structures in liquid water, Journal of the American Chemical Society 142 (6) (2020) 2868–2875.

[54] K. A. Silverstein, A. Haymet, K. A. Dill, The strength of hydrogen bonds in liquid water and around nonpolar solutes, Journal of the American Chemical Society 122 (33) (2000) 8037–8041.

[55] A. Kuffel, J. Zielkiewicz, Why the solvation water around proteins is more dense than bulk water, The Journal of Physical Chemistry B 116 (40) (2012) 12113–12124.

[56] F. Sterpone, M. Ceccarelli, M. Marchi, Dynamics of hydration in hen egg white lysozyme, Journal of molecular biology 311 (2) (2001) 409–419.

[57] S. Mathesan, A. Rath, P. Ghosh, Insights on Water Dynamics in the Hygromorphic Phenomenon of Biopolymer Films, Journal of Physical Chemistry B 121 (16) (2017) 4273–4282. doi:10.1021/acs.jpcb.7b00980.

[58] Y. M. Rhee, E. J. Sorin, G. Jayachandran, E. Lindahl, V. S. Pande, Simulations of the role of water in the protein-folding mechanism, Proceedings of the National Academy of Sciences 101 (17) (2004) 6456–6461.

[59] K. F. Rinne, J. C. Schulz, R. R. Netz, Impact of secondary structure and hydration water on the dielectric spectrum of poly-alanine and possible relation to the debate on slaved versus slaving water, The Journal of chemical physics 142 (21) (2015) 06B606_1.

[60] A. T. Kuo, S. Urata, R. Koguchi, T. Sonoda, S. Kobayashi, M. Tanaka, Effects of Side-Chain Spacing and Length on Hydration States of Poly(2-methoxyethyl acrylate) Analogues: A

Molecular Dynamics Study, ACS Biomaterials Science and Engineering 7 (6) (2021) 2383–2391. doi:10.1021/acsbiomaterials.1c00388.

[61] A. T. Kuo, S. Urata, R. Koguchi, T. Sonoda, S. Kobayashi, M. Tanaka, Molecular Dynamics Study on the Water Mobility and Side-Chain Flexibility of Hydrated Poly(ω-methoxyalkyl acrylate)s, ACS Biomaterials Science and Engineering 6 (12) (2020) 6690–6700. doi:10.1021/acsbiomaterials.0c01220.

[62] A. T. Kuo, T. Sonoda, S. Urata, R. Koguchi, S. Kobayashi, M. Tanaka, Elucidating the Feature of Intermediate Water in Hydrated Poly(ω-methoxyalkyl acrylate)s by Molecular Dynamics Simulation and Differential Scanning Calorimetry Measurement, ACS Biomaterials Science and Engineering 6 (7) (2020) 3915–3924. doi:10.1021/acsbiomaterials.0c00746.

[63] A. T. Kuo, S. Urata, R. Koguchi, K. Yamamoto, M. Tanaka, Analyses of equilibrium water content and blood compatibility for Poly(2-methoxyethyl acrylate) by molecular dynamics simulation, Polymer 170 (February) (2019) 76–84. doi:10.1016/j.polymer.2019.03.001.
URL https://doi.org/10.1016/j.polymer.2019.03.001

[64] R. Kumar, J. R. Schmidt, J. L. Skinner, Hydrogen bonding definitions and dynamics in liquid water, J. Chem. Phys. 126 (20) (2007) 204107.

[65] M. Matsumoto, Relevance of hydrogen bond definitions in liquid water, J. Chem. Phys. 126 (5) (2007) 054503.

[66] D. Prada-Gracia, R. Shevchuk, F. Rao, The quest for self-consistency in hydrogen bond definitions, J. Chem. Phys. 139 (8) (2013) 084501.

[67] A. Ozkanlar, T. Zhou, A. E. Clark, Towards a unified description of the hydrogen bond network of liquid water: A dynamics based approach, J. Chem. Phys. 141 (21) (2014) 214107.

[68] D. Laage, J. T. Hynes, A Molecular Jump Mechanism of Water Reorientation, Science 311 (2006) 832–835.

[69] D. Laage, J. T. Hynes, On the Molecular Mechanism of Water Reorientation, J. Phys. Chem. B 112 (45) (2008) 14230–14242.

[70] R. H. Henchman, S. J. Irudayam, Topological hydrogen-bond definition to characterize the structure and dynamics of liquid water., J. Phys. Chem. B 114 (50) (2010) 16792–16810.

[71] R. H. Henchman, Water's dual nature and its continuously changing hydrogen bonds, J. Phys.: Condens. Matter 28 (38) (2016) 384001.

[72] F. H. Stillinger, Theory and Molecular Models for Water, Advances in Chemical Physics (Wiley-Blackwell,1975) 1–101.

[73] F. H. Stillinger, Water revisited, Science 209 (4455) (1980) 451–457.

[74] I. Ohmine, H. Tanaka, Fluctuation, relaxations, and hydration in liquid water. Hydrogen-bond rearrangement dynamics, Chem. Rev. 93 (7) (1993) 2545–2566.

[75] J. Teixeira, A. Luzar, S. Longeville, Dynamics of hydrogen bonds: how to probe their role in the unusual properties of liquid water, J. Phys.: Condens. Matter 18 (36) (2006) S2353–S2362.

[76] H. J. Bakker, J. L. Skinner, Vibrational Spectroscopy as a Probe of Structure and Dynamics in Liquid Water, Chem. Rev. 110 (3) (2010) 1498–1517.

[77] N. Agmon, Liquid Water: From Symmetry Distortions to Diffusive MotioN., Acc. Chem. Res. 45 (1) (2012) 63–73.

[78] F. Perakis, L. D. Marco, A. Shalit, F. Tang, Z. R. Kann, T. D. Kühne, R. Torre, M. Bonn, Y. Nagata, Vibrational Spectroscopy and Dynamics of Water, Chem. Rev. 116 (13) (2016) 7590–7607.

[79] T. Kawasaki, K. Kim, Classification of mobile- and immobile-molecule timescales for the Stokes–Einstein and Stokes–Einstein–Debye relations in supercooled water, J. Stat. Mech. 2019 (8) (2019) 084004.

[80] J. A. Hodgdon, F. H. Stillinger, Stokes-einstein violation in glass-forming liquids, Physical Review E 48 (1) (1993) 207.

[81] F. H. Stillinger, J. A. Hodgdon, Translation-rotation paradox for diffusion in fragile glass-forming liquids, Physical review E 50 (3) (1994) 2064.

[82] K. Ngai, Breakdown of debye-stokes-einstein and stokes-einstein relations in glass-forming liquids: An explanation from the coupling model, Philosophical Magazine B 79 (11-12) (1999) 1783–1797.

[83] D. Rapaport, Hydrogen bonds in water: Network organization and lifetimes, Mol. Phys. 50 (5) (1983) 1151–1162.

[84] A. Luzar, D. Chandler, Effect of Environment on Hydrogen Bond Dynamics in Liquid Water, Phys. Rev. Lett. 76 (6) (1996) 928–931.

[85] A. Luzar, D. Chandler, Hydrogen-bond kinetics in liquid water, Nature 379 (6560) (1996) 55–57.

[86] A. Luzar, Resolving the hydrogen bond dynamics conundrum, J. Chem. Phys. 113 (23) (2000) 10663.

[87] F. Sciortino, P. Poole, H. Stanley, S. Havlin, Lifetime of the bond network and gel-like anomalies in supercooled water, Phys. Rev. Lett. 64 (14) (1990) 1686–1689.

[88] F. W. Starr, J. K. Nielsen, H. E. Stanley, Fast and Slow Dynamics of Hydrogen Bonds in Liquid Water, Phys. Rev. Lett. 82 (11) (1999) 2294–2297.

[89] F. W. Starr, J. K. Nielsen, H. E. Stanley, Hydrogen-bond dynamics for the extended simple point-charge model of Water, Phys. Rev. E 62 (1) (2000) 579–587.

[90] H. F. M. C. Martiniano, N. Galamba, Insights on Hydrogen-Bond Lifetimes in Liquid and Supercooled Water, J. Phys. Chem. B 117 (50) (2013) 16188–16195.

[91] F. Sciortino, A. Geiger, H. E. Stanley, Effect of defects on molecular mobility in liquid water, Nature 354 (6350) (1991) 218–221.

[92] F. Sciortino, A. Geiger, H. E. Stanley, Network defects and molecular mobility in liquid water, J. Chem. Phys. 96 (5) (1992) 3857–3865.

[93] G. Stirnemann, D. Laage, Communication: On the origin of the non-Arrhenius behavior in water reorientation dynamics, J. Chem. Phys. 137 (3) (2012) 031101.

[94] S. Saito, I. Ohmine, B. Bagchi, Frequency dependence of specific heat in supercooled liquid water and emergence of correlated dynamics, J. Chem. Phys. 138 (9) (2013) 094503.

[95] L. Berthier, G. Biroli, J. Bouchaud, L. Cipelletti, W. van Saarloos (Eds.), Dynamical Heterogeneities in Glasses, Colloids, and Granular Media, Oxford University Press, USA, 2011.

[96] C. A. Angell, Glass formation and glass transition in supercooled liquids, with insights from study of related phenomena in crystals, J. Non-Cryst. Solids 354 (42–44) (2008) 4703–4712.

[97] F. H. Stillinger, A Topographic View of Supercooled Liquids and Glass FormatioN., Science 267 (5206) (1995) 1935–1939.

[98] P. G. Debenedetti, F. H. Stillinger, Supercooled liquids and the glass transitioN., Nature 410 (2001) 259–267.

[99] D. Prada-Gracia, R. Shevchuk, P. Hamm, F. Rao, Towards a microscopic description of the free-energy landscape of Water, J. Chem. Phys. 137 (14) (2012) 144504–144504–7.

[100] T. Morawietz, A. Singraber, C. Dellago, J. Behler, How van der Waals interactions determine the unique properties of Water, Proc. Natl. Acad. Sci. U.S.A. 113 (30) (2016) 8368–8373.

[101] M. Chen, H. Ko, R. C. Remsing, M. F. C. Andrade, B. Santra, Z. Sun, A. Selloni, R. Car, M. L. Klein, J. P. Perdew, X. Wu, Ab initio theory and modeling of Water, Proc. Natl. Acad. Sci. U.S.A. 114 (41) (2017) 10846–10851.

[102] P. G. Bolhuis, C. Dellago, D. Chandler, Sampling ensembles of deterministic transition pathways, Faraday Disc. 110 (1998) 421–436.

[103] P. L. Geissler, C. Dellago, D. Chandler, Kinetic Pathways of Ion Pair Dissociation in Water, J. Phys. Chem. B 103 (18) (1999) 3706–3710.

[104] P. G. Bolhuis, C. Dellago, D. Chandler, Reaction coordinates of biomolecular isomerization, Proc. Natl. Acad. Sci. U.S.A. 97 (11) (2000) 5877–5882.

[105] F. S. Csajka, D. Chandler, Transition pathways in a many-body system: Application to hydrogen-bond breaking in water, J. Chem. Phys. 109 (3) (1998) 1125–1133.

[106] D. Chandler, Statistical mechanics of isomerization dynamics in liquids and the transition state approximatioN., J. Chem. Phys. 68 (6) (1978) 2959.

[107] P. Hänggi, P. Talkner, M. Borkovec, Reaction-rate theory: fifty years after Kramers, Rev. Mod. Phys. 62 (2) (1990) 251–341.

[108] W. L. Jorgensen, J. Chandrasekhar, J. D. Madura, R. W. Impey, M. L. Klein, Comparison of simple potential functions for simulating liquid water, J. Chem. Phys. 79 (2) (1983) 926.

[109] C. Vega, J. L. F. Abascal, Simulating water with rigid non-polarizable models: a general perspective, Phys. Chem. Chem. Phys. 13 (44) (2011) 19663.

[110] B. Hess, C. Kutzner, D. van der Spoel, E. Lindahl, GROMACS 4: Algorithms for Highly Efficient, Load-Balanced, and Scalable Molecular Simulation, J. Chem. Theory Comput. 4 (3) (2008) 435–447.

[111] M. J. Abraham, T. Murtola, R. Schulz, S. Páll, J. C. Smith, B. Hess, E. Lindahl, GROMACS: High performance molecular simulations through multi-level parallelism from laptops to supercomputers, SoftwareX 1-2 (2015) 19–25.

[112] O. Conde, J. Teixeira, Depolarized Light-Scattering of Heavy-Water, and Hydrogen-Bond Dynamics, Mol. Phys. 53 (4) (1984) 951–959.

[113] J. Teixeira, M. C. Bellissent-Funel, S. H. Chen, A. J. Dianoux, Experimental determination of the nature of diffusive motions of Water molecules at low temperatures, Phys. Rev. A 31 (3) (1985) 1913–1917.

[114] R. Laenen, C. Rauscher, A. Laubereau, Local Substructures of Water Studied by Transient Hole-Burning Spectroscopy in the Infrared: Dynamics and Temperature Dependence, J. Phys. Chem. B 102 (46) (1998) 9304–9311.

[115] H. E. Stanley, L. Cruz, S. T. Harrington, P. H. Poole, S. Sastry, F. Sciortino, F. W. Starr, R. Zhang, Cooperative molecular motions in water: The liquid-liquid critical point hypothesis, Physica A 236 (1) (1997) 19–37.

[116] E. R. Weeks, D. A. Weitz, Properties of Cage Rearrangements Observed near the Colloidal Glass TransitioN., Phys. Rev. Lett. 89 (2002) 095704.

[117] K. S. Schweizer, E. J. Saltzman, Activated Hopping, Barrier Fluctuations, and Heterogeneity in Glassy Suspensions and Liquids, J. Phys. Chem. B 108 (51) (2004) 19729–19741.

[118] H. Shiba, T. Kawasaki, A. Onuki, Relationship between bond-breakage correlations and four-point correlations in heterogeneous glassy dynamics: configuration changes and vibration modes., Phys. Rev. E 86 (4) (2012) 041504.

[119] M. P. Ciamarra, R. Pastore, A. Coniglio, Particle jumps in structural glasses., Soft Matter 12 (2) (2016) 358–366.

[120] R. Pastore, G. Pesce, A. Sasso, M. P. Ciamarra, Cage Size and Jump Precursors in Glass-Forming Liquids: Experiment and Simulations, J. Phys. Chem. Lett. 8 (7) (2017) 1562–1568.

[121] M. G. Mazza, N. Giovambattista, H. E. Stanley, F. W. Starr, Connection of translational and rotational dynamical heterogeneities with the breakdown of the Stokes-Einstein and Stokes-Einstein-Debye relations in water., Phys. Rev. E 76 (3) (2007) 031203.

[122] E. Guillaud, S. Merabia, D. de Ligny, L. Joly, Decoupling of viscosity and relaxation processes in supercooled water: a molecular dynamics study with the TIP4P/2005f model, Phys. Chem. Chem. Phys. 19 (3) (2017) 2124–2130.

[123] P. Montero de Hijes, E. Sanz, L. Joly, C. Valeriani, F. Caupin, Viscosity and self-diffusion of supercooled and stretched water from molecular dynamics simulations, J. Chem. Phys. 149 (9) (2018) 094503.

[124] T. Kikutsuji, K. Kim, N. Matubayasi, How do hydrogen bonds break in supercooled water?: Detecting pathways not going through saddle point of two-dimensional potential of mean force, J. Chem. Phys. 148 (24) (2018) 244501.

[125] T. Kikutsuji, K. Kim, N. Matubayasi, Diffusion dynamics of supercooled water modeled with the cage-jump motion and hydrogen-bond rearrangement, J. Chem. Phys. 150 (20) (2019) 204502.

[126] E. W. Montroll, G. H. Weiss, Random Walks on Lattices. II, J. Math. Phys. 6 (2) (1965) 167–181.

[127] K. Vollmayr-Lee, Single particle jumps in a binary Lennard-Jones system below the glass transition, J. Chem. Phys. 121 (10) (2004) 4781.

[128] L. Berthier, D. Chandler, J. P. Garrahan, Length scale for the onset of Fickian diffusion in supercooled liquids, EPL 69 (2005) 320.

[129] P. Chaudhuri, L. Berthier, W. Kob, Universal Nature of Particle Displacements close to Glass and Jamming Transitions, Phys. Rev. Lett. 99 (2007) 060604.

[130] E. J. Saltzman, K. S. Schweizer, Large-amplitude jumps and non-Gaussian dynamics in highly concentrated hard sphere fluids, Phys. Rev. E 77 (5) (2008) 051504.

[131] T. Kawasaki, A. Onuki, Slow relaxations and stringlike jump motions in fragile glass-forming liquids: Breakdown of the Stokes-Einstein relation, Phys. Rev. E 87 (1) (2013) 012312.

[132] F. W. Starr, J. F. Douglas, S. Sastry, The relationship of dynamical heterogeneity to the Adam-Gibbs and random first-order transition theories of glass formation, J. Chem. Phys. 138 (12) (2013) 12A541.

[133] F. Puosi, C. De Michele, D. Leporini, Scaling between relaxation, transport and caged dynamics in a binary mixture on a per-component basis, J. Chem. Phys. 138 (12) (2013) 12A532.

[134] J. Helfferich, F. Ziebert, S. Frey, H. Meyer, J. Farago, A. Blumen, J. Baschnagel, Continuous-time random-walk approach to supercooled liquids. I. Different definitions of particle jumps and their consequences, Phys. Rev. E 89 (4) (2014) 042603.

[135] J.-H. Hung, T. K. Patra, V. Meenakshisundaram, J. H. Mangalara, D. S. Simmons, Universal localization transition accompanying glass formation: insights from efficient molecular dynamics simulations of diverse supercooled liquids, Soft Matter 410 (Part 1) (2019) 259.

[136] A. H. Marcus, J. Schofield, S. A. Rice, Experimental observations of non-Gaussian behavior and stringlike cooperative dynamics in concentrated quasi-two-dimensional colloidal liquids, Phys. Rev. E 60 (1999) 5725–5736.

[137] E. R. Weeks, J. Crocker, A. C. Levitt, A. Schofield, D. Weitz, Three-Dimensional Direct Imaging of Structural Relaxation Near the Colloidal Glass Transition, Science 287 (2000) 627–631.

[138] E. R. Weeks, D. A. Weitz, Subdiffusion and the cage effect studied near the colloidal glass transition, Chem. Phys. 284 (1-2) (2002) 361–367.

[139] W. van Megen, H. J. Schöpe, The cage effect in systems of hard spheres, J. Chem. Phys. 146 (10) (2017) 104503.

[140] R. Pastore, A. Coniglio, M. Pica Ciamarra, From cage-jump motion to macroscopic diffusion in supercooled liquids, Soft Matter 10 (31) (2014) 5724–5728.

[141] R. Pastore, A. Coniglio, M. P. Ciamarra, Dynamic phase coexistence in glass–forming liquids, Sci. Rep. 5 (1) (2015) 2827.

[142] R. Pastore, A. Coniglio, M. P. Ciamarra, Spatial correlations of elementary relaxation events in glass-forming liquids, Soft Matter 11 (36) (2015) 7214–7218.

[143] R. Pastore, A. Coniglio, A. de Candia, A. Fierro, M. Pica Ciamarra, Cage-jump motion reveals universal dynamics and non-universal structural features in glass forming liquids, J. Stat. Mech. 2016 (5) (2016) 054050.

[144] J. L. F. Abascal, C. Vega, A general purpose model for the condensed phases of water: TIP4P/2005, J. Chem. Phys. 123 (23) (2005) 234505.

[145] R. S. Singh, J. W. Biddle, P. G. Debenedetti, M. A. Anisimov, Two-state thermodynamics and the possibility of a liquid-liquid phase transition in supercooled TIP4P/2005 water, J. Chem. Phys. 144 (14) (2016) 144504.

[146] J. W. Biddle, R. S. Singh, E. M. Sparano, F. Ricci, M. A. Gonzalez, C. Valeriani, J. L. F. Abascal, P. G. Debenedetti, M. A. Anisimov, F. Caupin, Two-structure thermodynamics for the TIP4P/2005 model of water covering supercooled and deeply stretched regions, J. Chem. Phys. 146 (3) (2017) 034502.

[147] M. De Marzio, G. Camisasca, M. Rovere, P. Gallo, Microscopic origin of the fragile to strong crossover in supercooled water: The role of activated processes, J. Chem. Phys. 146 (8) (2017) 084502.

[148] I.-C. Yeh, G. Hummer, System-Size Dependence of Diffusion Coefficients and Viscosities from Molecular Dynamics Simulations with Periodic Boundary Conditions, J. Phys. Chem. B 108 (40) (2004) 15873–15879.

[149] E. Shiratani, M. Sasai, Growth and collapse of structural patterns in the hydrogen bond network in liquid water, J. Chem. Phys. (1996).

[150] E. Shiratani, M. Sasai, Molecular scale precursor of the liquid–liquid phase transition of water, J. Chem. Phys. 108 (8) (1998) 3264–3276.

[151] M. J. Cuthbertson, P. H. Poole, Mixturelike Behavior Near a Liquid-Liquid Phase Transition in Simulations of Supercooled Water, Phys. Rev. Lett. 106 (11) (2011) 91.

[152] R. Shi, H. Tanaka, Microscopic structural descriptor of liquid water, J. Chem. Phys. 148 (12) (2018) 124503.

[153] A. Rahman, F. H. Stillinger, Molecular Dynamics Study of Liquid Water, J. Chem. Phys. 55 (7) (1971) 3336–3359.

[154] R. L. Blumberg, H. E. Stanley, A. Geiger, P. Mausbach, Connectivity of hydrogen bonds in liquid water, J. Chem. Phys. 80 (10) (1984) 5230.

[155] F. Sciortino, S. L. Fornili, Hydrogen bond cooperativity in simulated water: Time dependence analysis of pair interactions, J. Chem. Phys. 90 (5) (1989) 2786–2792.

[156] B. Jana, R. S. Singh, B. Bagchi, String-like propagation of the 5-coordinated defect state in supercooled water: molecular origin of dynamic and thermodynamic anomalies, Phys. Chem. Chem. Phys. 13 (36) (2011) 16220–16226.

[157] E. Guillaud, L. Joly, D. de Ligny, S. Merabia, Assessment of elastic models in supercooled water: A molecular dynamics study with the TIP4P/2005f force field, J. Chem. Phys. 147 (1) (2017) 014504.

[158] G. Camisasca, N. Galamba, K. T. Wikfeldt, L. G. M. Pettersson, Translational and rotational dynamics of high and low density TIP4P/2005 water, J. Chem. Phys. 150 (22) (2019) 224507.

[159] S. Naserifar, W. A. Goddard, III, Anomalies in Supercooled Water at textasciitilde 230 K Arise from a 1D Polymer to 2D Network Topological Transformation, J. Phys. Chem. Lett. 10 (20) (2019) 6267–6273.

[160] R. Horstmann, M. Vogel, Relations between thermodynamics, structures, and dynamics for modified water models in their supercooled regimes, J. Chem. Phys. 154 (5) (2021) 054502.

[161] T. Kawasaki, K. Kim, Spurious violation of the Stokes–Einstein–Debye relation in supercooled water, Sci. Rep. 9 (1) (2019) 8118.

[162] T. Kikutsuji, K. Kim, N. Matubayasi, Consistency of geometrical definitions of hydrogen bonds based on the two-dimensional potential of mean force with respect to the time correlation in liquid water over a wide range of temperatures, J. Mol. Liq. 294 (2019) 111603.

[163] G. R. Bowman, V. S. Pande, F. Noé (Eds.), An Introduction to Markov State Models and Their Application to Long Timescale Molecular Simulation, Vol. 797 of Advances in Experimental Medicine and Biology, Springer Netherlands, Dordrecht, 2014.

[164] G. R. Bowman, K. A. Beauchamp, G. Boxer, V. S. Pande, Progress and challenges in the automated construction of Markov state models for full protein systems, J. Chem. Phys. 131 (12) (2009) 124101.

[165] F. Noé, C. Schutte, E. Vanden-Eijnden, L. Reich, T. R. Weikl, Constructing the equilibrium ensemble of folding pathways from short off-equilibrium simulations, Proc. Natl. Acad. Sci. U.S.A. 106 (45) (2009) 19011–19016.

[166] V. S. Pande, K. Beauchamp, G. R. Bowman, Everything you wanted to know about Markov State Models but were afraid to ask, Methods 52 (1) (2010) 99–105.

[167] J.-H. Prinz, H. Wu, M. Sarich, B. Keller, M. Senne, M. Held, J. D. Chodera, C. Schütte, F. Noé, Markov models of molecular kinetics: Generation and validation, J. Chem. Phys. 134 (17) (2011) 174105.

[168] J.-H. Prinz, B. Keller, F. Noé, Probing molecular kinetics with Markov models: metastable states, transition pathways and spectroscopic observables, Phys. Chem. Chem. Phys. 13 (38) (2011) 16912–16927.

[169] T. J. Lane, G. R. Bowman, K. Beauchamp, V. A. Voelz, V. S. Pande, Markov state model reveals folding and functional dynamics in ultra-long MD trajectories., J. Am. Chem. Soc. 133 (45) (2011) 18413–18419.

[170] J. D. Chodera, F. Noé, Markov state models of biomolecular conformational dynamics., Curr. Opin. Struct. Biol 25 (2014) 135–144.

[171] D. Shukla, C. X. Hernández, J. K. Weber, V. S. Pande, Markov State Models Provide Insights into Dynamic Modulation of Protein Function, Acc. Chem. Res. 48 (2) (2015) 414–422.

[172] C. Gu, H.-W. Chang, L. Maibaum, V. S. Pande, G. E. Carlsson, L. J. Guibas, Building Markov state models with solvent dynamics, BMC Bioinformatics 14 (2) (2013) 1–9.

[173] P. Hamm, Markov state model of the two-state behaviour of water, J. Chem. Phys. 145 (13) (2016) 134501.

[174] R. Schulz, Y. von Hansen, J. O. Daldrop, J. Kappler, F. Noé, R. R. Netz, Collective hydrogen-bond rearrangement dynamics in liquid water, J. Chem. Phys. 149 (24) (2018) 244504.

[175] F. Martelli, Unravelling the contribution of local structures to the anomalies of water: The synergistic action of several factors, J. Chem. Phys. 150 (9) (2019) 094506.

List of Publications

Main papers:

1. T. Kikutsuji, K. Kim, and N. Matubayasi, "How do hydrogen bonds break in supercooled water?: Detecting pathways not going through the saddle point of two-dimensional potential of mean force", *The Joural of Chemical Physics* **148**, 244501(8 pages) (2018). https://doi.org/10.1063/1.5033419

2. T. Kikutsuji, K. Kim, and N. Matubayasi,"Consistency of geometrical definitions of hydrogen bonds based on the two-dimensional potential of mean force with respect to the time correlation in liquid water over a wide range of temperatures", *Journal of Molecular Liquids* **249**, 11603(6 pages) (2019). https://doi.org/10.1016/j.molliq.2019.111603

3. T. Kikutsuji, K. Kim, and N. Matubayasi, "Diffusion dynamics of supercooled water modeled with the cage-jump motion and hydrogen-bond rearrangement", *The Journal of Chemical Physics* **150**, 204502(6 pages) (2019). https://doi.org/10.1063/1.5095978

4. T. Kikutsuji, K. Kim, and N. Matubayasi, "Transition pathway of hydrogen bond switching in supercooled water analyzed by the Markov state model", *The Journal of Chemical Physics* **154**, 234501(7 pages) (2021). https://doi.org/10.1063/5.0055531

Related paper:

1. R. Pastore, T. Kikutsuji, F. Rusciano, N. Matubayasi, K. Kim, and F. Greco, "Breakdown of the Stokes-Einstein relation in supercooled liquids: A cage-jump perspective", *The Journal of Chemical Physics*, **155**, 114503(7 pages) (2021). https://doi.org/10.1063/5.0059622

Acknowledgements

The author is greatly indebted to Professor Nobuyuki Matubayasi and Associate Professor Kang Kim for their constant guidance and helpful advice throughout this work. I am grateful to Research Associate Professor Takuma Yagasaki and Assistant Professor Kento Kasahara of Osaka University for valuable discussions.

I also acknowledge all members of the Matubayasi laboratory for their friendship. Special thanks are given to the following colleagues for discussions: Professor Francesco Greco, Assistant Professor Raffaele Pastore, Specially Appointed Lecturer Yoshiki Ishii, Dr. Kazuo Yamada, Dr. Hidekazu Kojima, and Dr. Simon Hikiri.

I was supported by JSPS KAKENHI Grant No. JP20J14619, JSPS Fellows, and the Program for Leading Graduate Schools "Interactive Materials Science Cadet Program." The numerical calculations were performed at the Research Center for Computational Science, Okazaki Research Facilities, National Institutes of Natural Sciences and at the Cybermedia Center, Osaka University. Finally, I sincerely wishes to thank my family for their moral support and warm encouragements.

Takuma Kikutsuji

Division of Chemical Engineering

Graduate School of Engineering Science

Osaka University, Toyonaka, Osaka 560-8531, Japan